Auxin promotes GPI-anchored protein-mediated trafficking of ABP1 to enable cell-surface auxin signaling

Jing Wang[1,2,3], Jiang-ping Ye[1,2,3], Minmin Zhang[1], Hanqian Feng[1], Mengzhen Liu[1], Yuanzhi Huang[1,2], Tongda Xu[4], Baiyan Lu[1], Chao Li[1,2,3,*]

Affiliations:

[1]School of Life Sciences, East China Normal University, Shanghai, 200241, China.

[2]Institute of Advanced Agricultural Science and Technology, East China Normal University, Shanghai, 200241, China.

[3]Institute of Eco-Chongming, East China Normal University, Shanghai, 202162, China.

[4]Haixia Institute of Science and Technology, and College of Life Sciences, Fujian Agriculture and Forestry University, Fuzhou, Fujian 350002, China.

*Corresponding author. Email: cli@bio.ecnu.edu.cn

Present addresses:

Baiyan Lu, College of Life Science, Northwest Normal University, Lanzhou, 730070, China.

Summary

Cell surface auxin signaling is essential for rapid cellular and growth responses to auxin. Auxin-Binding Protein 1 (ABP1) has been proposed as an extracellular auxin receptor, yet how the ER-retained ABP1 reaches the apoplast to function as an extracellular auxin receptor remains unclear. Here, we show that the *abp1* mutants had strong phenotype in the dark-triggered hypocotyl elongation in *Arabidopsis*. More interestingly, the dark-induced auxin drives ABP1 relocation from the ER to the plasma membrane (PM) through a LORELEI-like GPI-anchored protein 1 (LLG1)-based mechanism. Auxin promotes LLG1 expression and its interaction with ABP1, facilitating ABP1 trafficking via a GPI-AP-specific pathway. Upon reaching the apoplast, ABP1 dissociates from LLG1 under acidic conditions, enabling its competence for auxin perception and activation of the cell surface signaling. Together, our results uncover a GPI-AP-mediated transport mechanism for ABP1 auxin receptor and refine the molecular framework of cell-surface auxin perception.

Key words: auxin receptor ABP1, dark-induced hypocotyl elongation, cell surface auxin signaling, LLG1, GPI-anchored protein

Introduction

Auxin orchestrates pleiotropic biological processes involved in plant growth and development, influencing a wide range of events from cell elongation and differentiation to organ patterning (Aryal et al., 2020; Vanneste and Friml, 2009). It has been well characterized that canonical transcriptional auxin signaling pathway relies on the TIR1/AFB–Aux/IAA–ARF pathway for the regulation of auxin-responsive genes' expression (Dharmasiri et al., 2005; Kepinski and Leyser, 2005; Lavy and Estelle, 2016). Besides the transcriptional regulations occurring in nucleus, auxin also induces rapid non-transcriptional responses in apoplast within minutes, such as proton extrusion (Lin et al., 2021), membrane depolarization (Serre et al., 2021), calcium transients (Dubey et al., 2023), and cytoplasmic streaming (Kuhn et al., 2024), thereby contributing to immediate cellular and growth responses (Dubey et al., 2021; Fiedler and Friml, 2023). During the past decades, a key regulator of rapid auxin responses was isolated from maize and identified as AUXIN BINDING PROTEIN 1 (ABP1) based on its particular auxin-binding capacity (R. Hertel, 1972; Tian et al., 1995). Since then, ABP1 has been considered the best candidate for auxin receptor mediating fast auxin responses in apoplast (Eui-Jeon Woo, 2002; Löbler and Klämbt, 1985; Shoji SHIMOMURA, 1986; Xu et al., 2010). Unfortunately, the lack of obvious morphological phenotypes in *abp1* knockout mutant led to longstanding controversy over its function (Gao et al., 2015). More recently, the function of ABP1 as an auxin receptor is confirmed, which from an auxin-sensing complex with TRANSMEMBRANE KINASE receptor-like kinase 1 (TMK1) in an auxin-dependent manner,

mediating wound-triggered vascular formation and regeneration (Friml et al., 2022). In addition to ABP1, ABP1-like 1/2 also participate in TMKs-mediated auxin signaling and regulate developmental processes, including pavement cell interdigitation and hypocotyl elongation, indicating partially overlapping yet distinct roles of ABP1/ABLs in rapid auxin responses (Yu et al., 2023). Recent research has further demonstrated that the ABP1/ABL3–TMK1 cell-surface pathway further controls PIN2-mediated auxin fluxes required for root gravitropism (Rodriguez et al., 2025).

Paradoxically, the functional assignment of ABP1 at the cell surface contrasts with its predominant subcellular localization. ABP1 contains a C-terminal KDEL motif that confers its retention in the endoplasmic reticulum (ER), and it is confirmed that the majority of ABP1 protein resides in the ER lumen under steady-state conditions (Jones and Herman, 1993). Intriguingly, it has been found that treatment of indole-3-acetic acid (IAA) and synthetic auxin 2,4-D induces the secretion of ABP1 from ER to apoplast in *Arabidopsis* root cells and *Zea mays* BMS cells (Friml et al., 2022; Jones and Herman, 1993). Biochemically, ABP1 exhibits high binding affinity to IAA at acidic pH (15.1 ± 0.012 μM at pH 5.5), but dramatically reduced affinity at near-neutral pH (1,350 ± 150 μM at pH 7.6) (Friml et al., 2022; Tian et al., 1995). Corelating to the near-neutral pH in ER and the relatively acidic pH in apoplast, ABP1 is believed to regulate fast auxin responses in cell surface for global phosphorylation (Friml et al., 2022). Nevertheless, a fundamental mechanistic question remains unresolved: how does auxin overcome ER retention and direct the trafficking of ABP1 from intracellular compartments to the apoplast, thereby initiating rapid cellular responses (Friml, 2022; Friml et al., 2022; Napier, 2021).

Clues to the ABP1 trafficking conundrum may lie in its interaction partners at the cell surface. Glycosylphosphatidylinositol-anchored protein (GPI-AP) represent a distinct class of secreted proteins with high transportation efficiency, which are tethered to the outer leaflet of the PM, where their high lateral mobility allows rapid redistribution and dynamic interactions with other membrane signaling components (Fujita and Kinoshita, 2012; Fujita et al., 2011; Maeda and Kinoshita, 2011; Zhang and Fujita, 2024). Early studies reported an interaction between ABP1 and the GPI-anchored protein SKU5 (Shimomura, 2006), raising the possibility that GPI-APs contribute to ABP1 export. Plant-specific LORELEI (LRE) family GPI-APs, including LRE and LLG1/2/3, function as chaperones that direct the trafficking of CrRLK1L receptor kinases and serves as coreceptors in the RALF peptides signaling during plant development (Chao Li, 2015; Feng et al., 2019). Moreover, LLG1 has emerged as a versatile chaperone that facilitates the immune receptor kinases LET1/2 to the PM and participate in immune responses as a coreceptor (Chen et al., 2022; Huang et al., 2020; Qiujing Shena, 2017). Recent findings also demonstrate that LLG1 participates in the auxin stimulated ROS/NO accumulation through cell surface FERONIA–RAC/ROP pathway, which stimulates the oxidation-/nitrosylation-mediated TIR1/AFB2 nuclear transport and thus

transcriptional auxin responses (Lu et al., 2024). It would worthwhile to examine whether LLG1 has the capacity to facilitate ABP1 trafficking.

In this study, we disclose that LLG1 chaperones the secretion of ABP1 from the endoplasmic reticulum (ER) in an auxin-dependent manner. The interaction between ABP1 and LLG1 is pH-dependent. Therefore, upon reaching the PM, the ABP1-LLG1 interaction loosens due to the acidic environment of the apoplast and TMKs–AHAs-mediated apoplast acidification and hypocotyl elongation. Our work establishes that ABP1 employs a GPI-AP-mediated trafficking pathway to reach the apoplast, thereby resolving the long-standing enigma of ABP1 localization.

Results

ABP1 participates in dark-induced hypocotyl elongation

Although *ABP1* overexpression induces diverse auxin-related developmental abnormalities, the absence of clear phenotypes in *abp1* loss-of-function mutants has long impeded comprehensive understanding of *ABP1* function in auxin signaling and plant development (Gelova et al., 2021). Here, we generated the *pABP1:ABP1-eGFP* transgenic lines and found that the expression of ABP1 in the hypocotyl epidermis and cortex exhibited temporal variation, with markedly higher levels observed between days 4 to 5 (Figure S1A). Consistent with the fluorescence observations, RT-qPCR analysis further confirmed these expression patterns (Figure S1B). Notably, when we treated 4-day-old *Arabidopsis* seedlings grown under normal long-day photoperiod (16 h light/8 h dark) with darkness for 36 h, both *abp1-c1* and *abp1-TD1* mutant lines displayed significantly longer hypocotyls compared with wild type (WT) (Figure 1A). In line with this observation, growth kinetics analysis using a dual-point tracking assay (Huang et al., 2022) revealed that hypocotyl elongation proceeded through two clearly distinguishable phases: an initial fast-growing phase followed by a slower, sustained growth phase. Throughout the growth period, both *abp1* mutants exhibited significantly increased newly formed growth as well as higher rates of hypocotyl growth compared with the WT. Specifically, *abp1-c1* maintained accelerated growth throughout the entire monitoring period, whereas *abp1-TD1* displayed rapid elongation only during the early phase (comparable to *abp1-c1*) followed by a gradual decline in growth rate during later stages. Ultimately, both mutants developed longer hypocotyls than WT, with the elongation phenotype being more pronounced in *abp1-c1* (Figure 1B). We then selected the upper region of the hypocotyl as a representative zone used in all subsequent cytological analyses (Figure S1C). Using this region for cell length examination, we found that under dark treatment, the cortical cell area of hypocotyl was significantly larger in both *abp1* mutants compared with WT (Figures 1C and S1D).

Next, we examined the subcellular localization of ABP1 using fluorescence intensity profile

and Pearson's correlation coefficient analysis. Under standard long-day photoperiod, *ABP1* signal peaks showed greater colocalization with the ER marker RFP-HDEL, than with the FM4-64 stained PM, manifesting the predominant localization of *ABP1* in the ER (Steffens, 2011) (Figure S1E). In contrast, after dark treatment for 16–18 h, majority of ABP1 fluorescent signal colocalized with the PM rather than the ER marker (Figure 1D). Consistently, the Pearson's correlation coefficient (*r*) of ABP1 signal with FM4-64 increased markedly to 0.71 after dark treatment, compared to 0.46 in mock conditions, suggesting a time-dependent re-localization of ABP1 from the ER to the PM (Figures S1F and S1G). Thus, this identification of the ABP1-regulated hypocotyl elongation process establishes an effective system for elucidating the molecular mechanisms underlying ABP1 function.

Darkness induces ABP1 trafficking through auxin biosynthesis in the hypocotyl

Previous study reported that darkness enhances the synthesis of auxin in cotyledon (Chen et al., 2016). Therefore, we quantified the content of free IAA in the aboveground tissue of 4-day-old seedling. A marked increase of IAA content was detected in the sample that exposed with 24 h darkness (Figure S2A). To further explore the underlying molecular basis, we performed RT-qPCR analysis of the same plant material subjected to a time-course dark treatment. As anticipated, the expression of key auxin biosynthesis genes was markedly upregulated (Mano and Nemoto, 2012). Specifically, the *Anthranilate Synthase Alpha1* (*ASA1)* and *Tryptophan Aminotransferase of Arabidopsis 1* (*TAA1)* reached peak expression around 2 h, whereas *YUCCAs* (*YUC3*/*8*/*9)* were strongly induced during 12–24 h (Figures 2A, 2B and S2B). Consistently, a 24 h dark incubation also stimulated the expression of *pYUC9:GUS* in hypocotyl, further confirming the transcriptional activation of *YUC9* (Figure S2C). In agreement with these findings, PPBo (*p*-phenoxyphenyl boronic acid) (Kakei et al., 2015) significantly suppressed darkness-induced hypocotyl elongation in WT seedlings. Notably, the pronounced differences observed in *abp1* mutant lines under dark conditions were largely eliminated upon PPBo treatment (Figures 2C and S2D). Known that the PIN family proteins-mediated polar auxin transport is essential for hypocotyl cell elongation (Hu et al., 2021; Luschnig and Friml, 2024), we performed the N-1-Naphthylphthalamic acid treatment (NPA, an inhibitor of PINs) (Yang et al., 2022). Surprisingly, *abp1* mutants exhibited a similar level of repression as WT hypocotyls, demonstrating that PINs-dependent auxin transport is strictly required for dark-induced hypocotyl elongation (Figure S2E). These findings suggest that darkness promotes auxin biosynthesis and thus the levels of auxin in hypocotyl, triggering ABP1-mediated hypocotyl elongation.

Given that the dark-induced phenotype of *abp1* is associated with increased auxin biosynthesis, we asked whether it might result from altered intracellular trafficking of ABP1. Upon treatment with

137 1 μM IAA or 10 μM NAA (naphthalene acetic acid, a synthetic auxin) for 1 h, the fluorescence
138 intensity profiles of ABP1-eGFP and FM4-64 staining were well aligned, in contrast to the distinct
139 patterns observed under mock conditions (Figure 2D). Three-dimensional surface plot analysis
140 further revealed the auxin treatment-triggered a redistribution of ABP1-eGFP from intracellular
141 compartment to the PM region (Figure 2D right). In addition, the Pearson's correlation coefficient
142 between ABP1-eGFP and FM4-64 significantly increased following either IAA or NAA treatment
143 (Figures 2E and S2E). Consistently, the proportion of PM-localized ABP1-eGFP in hypocotyl
144 epidermal cells was significantly higher in auxin-treated samples compared with mock treatment
145 (Figure 2F). In line with the microscopy observations, a marked reduction in ABP1 abundance was
146 detected in the ER protein fraction of IAA-treated samples compared with the mock (Figure 2G). In
147 contrast, total ABP1 levels remained unchanged under time- and concentration-dependent IAA
148 treatment, as well as upon co-treatment with MG132, an inhibitor of 26S proteasome (Figure S2F).
149 We next examined whether auxin biosynthesis influences ABP1 trafficking by analyzing its
150 localization in both WT and the *asa1* mutant. Following dark treatment, ABP1 largely remined in
151 intracellular compartments in the *asa1* mutant, in contrast to its prominent PM localization observed
152 in WT hypocotyl cells (Figure S2G). Together, these findings suggest that the darkness-induced
153 increase in auxin levels via biosynthesis drives the trafficking of ABP1 from the ER to the PM in
154 hypocotyl cells.

155 **Dark-induced LLG1 expression facilitates the trafficking of ABP1**

156 Given the functional studies of LRE family GPI-APs as chaperones that mediate protein trafficking
157 and the involvement of LLG1 in auxin signaling, we next aimed to investigate whether LRE/LLGs
158 participate in ABP1 secretion. Between the vegetative tissue expressed LRE and LLG1, LLG1
159 showed dramatically higher expression in hypocotyl (Figure S3A). In hypocotyl epidermis and
160 cortex of the *pLLG1:eGFP-LLG1* transgenic seedlings, the *eGFP-LLG1* fluorescence peaked
161 around day three to four, following a temporal pattern similar to *ABP1* (Figure S3B). To this end,
162 we examined the hypocotyl of *llg1-2* mutant and observed accelerated hypocotyl elongation
163 compared with WT after dark treatment (Figure 3A). Moreover, we set up a local IAA application
164 assay (dissolved in lanolin paste) to cotyledons (Bellstaedt et al., 2019) of 4-day-old seedlings and
165 found that all *abp1* and *llg1* mutants displayed longer hypocotyls than WT. Due to the comparable
166 phenotype of the *abp1* mutants with *llg1*, we conducted genetic crossing and obtained the double
167 mutant. We found that the *abp1-c1 llg1-2* double mutant displayed similar phenotype to that of either
168 single mutant (Figures 3B and S3C). These results suggest that ABP1 and LLG1 function
169 cooperatively in the regulation of auxin-induced hypocotyl elongation. To further investigate the
170 auxin–*LLG1* relationship, we performed a promoter analysis using PlantCARE (Lescot et al., 2002)
171 and identified an auxin-responsive TGA-element motif in the *LLG1* promoter region (Figure S3D).

Notably, dark treatment significantly induced the transcription of *LLG1* within 2–4 hours and the LLG1 protein also accumulated significantly under dark conditions compared with the untreated controls (Figure 3C–D). Consistently, the transcription of *LLG1* was significantly induced following 30 minutes of IAA treatment, and the LLG1 protein was highly enriched in the PM fraction thereafter (Figures 3D and S3E). These results demonstrate that dark-induced auxin promotes LLG1 expression through transcriptional regulation.

GPI modification serves as a major sorting signal for the delivery of GPI-APs to the PM in yeast, mammals, and plants (Muñiz and Riezman, 2016; Zavaliev et al., 2016). Myriocin (Myn), an inhibitor of ceramide synthesis, inhibits the remodeling of GPI anchors into inositolphosphoceramide (IPC)-containing forms by depleting the ceramide pool in yeast, thereby impairing the transport of GPI-APs from the ER to the Golgi apparatus (Horvath et al., 1994). The GPI anchors of plant GPI-APs also possess IPC tails (Xu et al., 2022), suggesting a similar ceramide-dependent remodeling process to that in yeast. We then examined whether Myn could disturb the function of GPI-Aps in plants. Through root hair growth observations, we found that Myn treatment effectively inhibited root hair growth, phenocopying various growth-arrested phenotypes of the *llg1-2* mutant (Figures S3F–G). Under Myn treatment, we observed obvious intracellular retention of LLG1 in growing root hairs, indicating that inhibition of GPI-AP trafficking impairs proper LLG1 localization (Figures 3E and S3H). These results suggest that, as a GPI-Aps, LLG1 may utilize this trafficking pathway to mediate the targeted localization of specific PM proteins. Moreover, we performed co-treatment with Myn and IAA to assess LLG1 subcellular localization and found that the eGFP-LLG1 signal was markedly retained within the ER in hypocotyl cells (Figures 3F). Quantitative analysis of PM signal intensity showed that IAA treatment increased eGFP-LLG1 accumulation at the PM, while co-treatment with Myn significantly attenuated LLG1 localization to PM (Figures 3G and S3I). In addition, total protein analysis by immunoblotting indicated that Myn and IAA co-treatment did not noticeably change overall LLG1 abundance, indicating that Myn specifically impacts its trafficking (Figure S3J).

Auxin stimulates the pH-dependent interaction between LLG1 and ABP1

We carried out structural modeling of $ABP1^{\Delta SP}$ and $LLG1^{core}$ using AlphaFold3 and identified a potential strong interaction interface. Residues within this predicted binding region showed pLDDT (predicted Local Distance Difference Test) scores exceeding 70, supporting the reliability of the modeled interface (Figure 4A). We then examined the interaction by co-immunoprecipitation (Co-IP) analysis using seedlings harboring both *pABP1:ABP1-eGFP* and *pLLG1:mCherry-LLG1-Flag* transgenes and detected strong interaction between ABP1-eGFP and mCherry-LLG1-Flag (Figure 4B). Moreover, luciferase-complementation assay (split-LUC) in *N. benthamiana* leaves also

206 demonstrated the interaction between full-length ABP1-nLuc and SP-cLuc-LLG1 (Figure S4A). In
207 particular, the ABP1$^{\Delta KDEL}$ (lacking the ER-retention KDEL motif) could interact with the LLG1$^{\Delta C}$
208 (deficient in GPI-anchor attachment), further confirming their interaction in the core regions
209 (Figures 4C and S4B).

210 To further determine whether the distinct pH environments of the ER (~pH 7.5) and the
211 apoplast (~pH 5.5) influence the ABP1–LLG1 interaction, we performed pull-down assays across a
212 pH gradient. Interestingly, ABP1$^{\Delta SP}$ and LLG1$^{\Delta SP}$ displayed a pronounced pH-dependent gradient,
213 with strong interactions were observed at pH 7.5 and pH 8.5 and markedly weaker interactions at
214 pH5.5 (Figure 4D). These results indicated that the ABP1–LLG1 interaction is preferentially
215 stabilized under ER-like neutral pH conditions and is disfavored in the acidic apoplast environment.
216 Subsequently, we employed an IAA concentration gradient ranging from 0 to 2.5 μM at pH 7.5 to
217 examine its effects on the interaction between ABP1 and LLG1. The results demonstrated an auxin
218 dose-dependent enhancement of their interaction, with stronger binding observed at higher IAA
219 concentrations (Figure 4E and S4C). However, this auxin-induced enhancement was not detected at
220 pH 5.5 (Figure S4D). Furthermore, we selected four ABP1 residues located at the interaction
221 interface based on the predicted ABP1$^{\Delta SP}$–LLG1^{core} structure—S106, T146, H148 and Q149—and
222 generated alanine-substituted ABP1 variants. Pull-down assays revealed that the H148A mutation
223 markedly weakened the interaction with LLG1$^{\Delta SP}$ compared with wild-type ABP1$^{\Delta SP}$ and other
224 variants. Furthermore, based on the closer spatial proximity between ABP-H148 and LLG-P113, we
225 also tested the effect of the P113 mutation (P113A) and detected dramatically reduced protein
226 interaction (Figure 4F).

227 To further investigate the function of auxin in the LLG1-mediated ABP1 transport, we
228 performed the pull-down assays using an auxin binding-pocket mutant of ABP1 (ABP1$^{M2X\Delta SP,}$
229 H59A/H61A) (Friml et al., 2022), and found that IAA failed to enhance its interaction with LLG1$^{\Delta SP}$
230 at either pH 7.5 or pH 5.5 (Figure S4C–D). Microscopy analyses also revealed that although 1 μM
231 IAA induced the partial translocation of *ABP1^{M2X}-eGFP* to the PM, the extent of this response was
232 markedly weaker than that of wild-type ABP1 (Figure 4G). Consistent to the biochemistry and
233 microscopy results, introduction of either *ABP1^{M2X}-eGFP* or *GFP-ABP1^{M2X}* under the native ABP1
234 promoter could not rescue the defective dark-induced hypocotyl elongation phenotype of the *abp1-*
235 *c1* mutant (Figure 4H). Altogether, these results indicate that auxin enhances the LLG1–ABP1
236 interaction in a dose-dependent manner, favoring the ER over the apoplast.

237 **LLG1 chaperones auxin-induced ABP1 transport through a GPI-AP trafficking pathway**

238 To investigate whether LLG1 mediates the translocation of ABP1, we co-expressed *pABP1:ABP1-*
239 *eGFP* with inducible *sp-mScarlet-LLG1 (XVE)* in *N. benthamiana* leaves. Consistent with the results

observed in seedlings, when ABP1-eGFP was expressing alone, the majority remained in the ER, and this localization was not affected by *β*-estradiol treatment. In contrast, IAA treatment induced significant transport to the PM (Figure S5A). Upon *β*-estradiol induction of *LLG1*, a substantial proportion of ABP1-eGFP colocalized with mScarlet-LLG1 at the PM, as marked by AHA2-eGFP (Figure S5B). In particular, this ABP1–LLG1 colocalization was further enhanced by auxin treatment. Given that H148 is crucial for the ABP1–LLG1 interaction, we transiently co-expressed *pABP1:ABP1*^{H148A}*-eGFP* together with *sp-mScarlet-LLG1 (XVE)* in tobacco leaves and conducted fluorescence imaging. Following *β*-estradiol-induced expression of mScarlet-LLG1 and auxin treatment, ABP1^{H148A}, in contrast to wild-type ABP1, was retained in the ER and failed to transport to the PM (Figures 5A–B). Moreover, we crossed the *pABP1:ABP1-eGFP* plants with *llg1-1* mutant and investigated the ABP1 transport. We found that auxin treatment failed to promote ABP1-eGFP translocation to the PM in the absence of LLG1 (Figures 5C–D and S5C). These findings demonstrate that LLG1 facilitates auxin-induced ABP1 trafficking via protein-protein interaction.

Given that LLG1 traffics through a GPI-AP-specific pathway, we next asked whether ABP1 secretion is dependent on the GPI-anchor of LLG1. GPI is synthesized in the ER from free phosphatidylinositol (PI) through a multistep process involving more than ten enzymatic reactions. The mature GPI anchor is then transferred en bloc to proteins, a process mediated by GPI transamidase, which cleaves the C-terminal tail and attaches the GPI moiety to the protein (Xu et al., 2022). We transiently co-expressed GPI-deficient *sp-mScarlet-LLG1*$^{\Delta C}$ *(XVE)* with *pABP1:ABP1-eGFP* in tobacco leaves and conducted fluorescence imaging. We observed that the florescent signals of ABP1-eGFP and mScarlet-LLG1$^{\Delta C}$ appear to be colocalized in the ER. However, unlike full-length LLG1, auxin treatment failed to trigger ABP1-eGFP–mScarlet-LLG1$^{\Delta C}$ secretion to the PM (Figure 5E). Consistent with the *llg1* mutant observations, co-treatment with GPI-AP trafficking inhibitor Myn also suppressed the effect of IAA treatment to promote the ABP1-eGFP secretion to the PM, and gave rise to some punctate structures reminiscent of the puncta of misfolded GPI-APs resulted from chemical-induced ER stress (Satpute-Krishnan et al., 2014) (Figure 5F and S5D–E). These results suggest that LLG1 relies on its GPI-anchor to facilitate the transportation of ABP1. In these observations, we noted that auxin-induced PM accumulation of ABP1 requires around half an hour. This timescale aligns with the phenotypic manifestation in *abp1* mutants, in which significant differences in hypocotyl elongation rates appear after 2.5 h of dark treatment. A similar pattern has been reported in roots, where PM-proximal aggregation of ABP1 is typically detected around 3 h after IAA treatment (Friml et al., 2022). We consider this kinetics reasonable, given that the *de novo* LLG1 synthesis and subsequent GPI-AP-dependent trafficking both play essential roles in ABP1 secretion.

ABP1 regulates AHA2-mediated apoplast acidification in dark-induced hypocotyl elongation

To further investigate the interaction between ABP1 and LLG1, we performed Förster resonance energy transfer-fluorescence lifetime imaging microscopy (FRET-FLIM) analysis. The donor-acceptor pair ABP1-mTurquoise2–LLG1-mVenus was transiently expressed in tobacco leaves. We observed that the co-expression of LLG1-mVenus marked reduced the fluorescence lifetime of ABP1-mTurquoise2 at both the ER and the PM. Notably, the FRET efficiency of the ABP1–LLG1 interaction was significantly higher in the ER (~60–80%) than at the PM (~40–60%) (Figure 6A). Moreover, given that ABP1 collaborates with TMK1/4 to regulate cell wall acidification through autoinhibited PM H^+-ATPases 1/2 (AHA1/2) (Friml et al., 2022; Lin et al., 2021), we examined the phenotypes of *aha1/2* mutants in our established dark-growth system. Both *aha1-7* and *aha2-4* mutants displayed shorter hypocotyl whereas a constitutively active AHA1 mutant, *ost2-2D* exhibited longer hypocotyl compared with WT (Figures S6A). Under IAA treatment, *aha2-4* and *ost2-2D* exhibited phenotypes resembling those observed under dark conditions, though *aha1-7* showed no significant difference from WT (Figure S6B). We further focused on AHA2 and generated the *abp1-c1 aha2-4* double mutant. This double mutant displayed dark-induced shorter hypocotyl similar to *aha2-4* (Figures 6C and S6C). These results linked the ABP1 to downstream AHA2 in the dark-promoted hypocotyl elongation.

We next applied the membrane-impermeable pH indicator HPTS (8-hydroxypyrene-1,3,6-trisulfonic acid trisodium salt) (Amali et al., 2011; Liu et al., 2025) and observed that dark treatment significantly reduced the apoplast pH in the hypocotyl epidermis and cortex (Figure S7A). Based on that, we further examined the apoplast pH in *abp1-c1* under dark conditions and discovered that the *abp1* apoplast was more acidic than that in the WT. Moreover, additional auxin treatment induced a rapid and pronounced acidification in WT apoplast; by contrast, the *abp1-c1* mutant failed to respond to auxin treatment (Figures 6D and S7B). Also, the pH measured by the HPTS-pH calibration consistent with this finding (Figure S7C–D). Nevertheless, no obvious differences were detected between WT and *abp1-c1* under light-grown conditions regarding auxin responses (Figure S7E). The phosphorylation of Thr947 in AHA2 acts as a molecular switch controlling proton pump activity to induced H^+ efflux[6,43,44]. When we applied IAA treatment under dark conditions, it rapidly increased the phosphorylation levels of AHA2 Thr947 in WT seedlings but not in the *abp1-c1* mutant (Figure 6E). Since the Thr881 has also been reported an activation site for the regulation of AHA2proton pump activity (Fuglsang et al., 2014; Lin et al., 2021), we introduced the *pAHA2:AHA2*$^{T881A/T947A}$ construct to the *aha2-4* background and found that this variant failed to rescue the dark-induced defective hypocotyl growth of *aha2-4* (Figure 6F). In addition, we applied Myn pretreatment before the treatment of dark and auxin for the investigation of LLG1 participation. Notably, the Myn application significantly disturbed the auxin-induced apoplast acidification in hypocotyl (Figures 6G and S7F). Furthermore, we also examined the Thr947 phosphorylation status

in the *llg1-2* mutant. Upon auxin treatment under dark conditions, however, this auxin-induced phosphorylation response was absent in *llg1-2*, mimicking the phenomenon observed in *abp1* mutant (Figure 6H). These results together establish a causal linkage between LLG1-facilitated ABP1 transport and AHA2-mediated apoplast acidification.

Discussion

Cell surface-mediated auxin signaling has long been recognized; however, the functional characterization of ABP1 as an auxin receptor remains largely unresolved. In particular, the mechanism by which auxin regulates the secretion of this ER-retained receptor to the apoplast, thereby initiating cell surface auxin signaling, has remained a mystery (Napier, 2021). In this study, by capture the critical expression peak of ABP1, we established an endogenous auxin induction system in which 4-day-old seedlings were subjected to 16–36 h of darkness, and observed pronounced hypocotyl elongation defects in *abp1* mutants. We found that this darkness induction system stimulates auxin synthesis and consequently upregulates LLG1 expression in hypocotyl cells. Using this system, we reveal that auxin promotes the interaction between LLG1 and ABP1 and facilitates their vesicular trafficking via a unique GPI-AP pathway. Upon reaching the outer leaflet of the PM, the ABP1 dissociates from the LLG1 due to the acidic pH and subsequently coordinates with TMK1/4–AHA1/2 pathway for hypocotyl elongation (Figure 7).

It has long been observed that auxin can induce the translocation of ABP1 to the apoplast; however, its binding affinity is low under the neutral condition of ER (Friml et al., 2022). This raises the question of how auxin functions in this process. In this study, our results show that IAA treatment enhances the ABP1-LLG1 interaction in a dose-dependent manner. Importantly, loss of auxin-binding capability in $ABP1^{M2X,}$ as well as disruption of LLG1, both lead to defects in dark/auxin-induced ABP1 transport. These findings demonstrate that ABP1-LLG1 complex acts as an auxin receptor in the ER. Previous structural analyses of ABP1 showed no major global conformational rearrangements upon auxin binding in crystal structures (Dahlke et al., 2009; Eui-Jeon Woo, 2002). Using Chai-1 molecule docking analysis, we found that, in addition to binding to the canonical pocket of ABP1, IAA could insert into the LLG1 protein. In certain working models, the predicted IAA binding sites locate close to the ABP1–LLG1 interaction interface (Figure S7H). This structural prediction provides a potential mechanistic explanation for how auxin regulate this process.

A central finding of this study is that the GPI-AP LLG1 promotes ABP1 secretion via a specialized GPI-AP trafficking pathway. In flowering plants, the C-terminal KDEL motif of ABP1 normally mediates its retrieval from the Golgi to the ER, thereby limiting its secretion (Jones and Herman, 1993). Our results indicate that auxin enables LLG1 to overcome this retention, facilitating the delivery of ABP1 to the apoplast where it can function in auxin perception and signaling. Several

mechanisms regarding to the release of ER-resident KDEL-bearing proteins have been hypothesized (Palazzo et al., 2022). Here we reveal the mechanism that auxin enables LLG1 to bypass the ER retention appears to happen through saturation of the KDEL receptor retrieval machinery caused by high LLG1 expression driving the ER exit of large amounts of ABP1, ultimately facilitating the delivery of ABP1 to the apoplast, where it participates in auxin perception and signaling. This mode of transport is distinct from conventional vesicular trafficking used by most membrane and secretory proteins and is characteristic of GPI-APs, which are sorted through sphingolipid-dependent membrane microdomains (Guillaume Alain Castillon, 2013). Such lipid-based sorting is thought to enhance trafficking efficiency and is conserved across eukaryotes (Zhang and Fujita, 2024). In addition, GPI-APs are tethered to the outer leaflet of the PM, conferring high lateral mobility that supports rapid redistribution during signaling events (Zhang and Fujita, 2024). Consistent with these properties, LLG1 may also contribute to the lateral organization of ABP1 at the PM, thereby facilitating its interaction with TMK1/4 receptor kinases and promoting downstream AHA1/2-mediated auxin signaling.

This study reveals that the interaction between LLG1 and ABP1 is regulated by pH, being strong under the near-neutral conditions of the ER but markedly weaker in the more acidic apoplastic environment. We found that auxin binding to ABP1 modulates its interaction with LLG1 in a manner that stabilizes the ABP1–LLG1 complex under neutral pH conditions. Upon secretion into the apoplast, the decrease in pH is expected to alter electrostatic interactions and local protein conformation, thereby weakening ABP1–LLG1 association and favoring a transition from ER-localized complex formation to interactions between ABP1 and TMK1/4 receptor kinases. We identified $ABP1^{H148}$ as a critical site for LLG1 interaction. The histidine residue can be reversible protonated under different pH conditions, leading to changes in hydrogen bond formation. Therefore, modification of H148 likely underlies the pH-dependent variation in ABP1–LLG1 binding affinity. Notably, this residue is essential for ABP1 trafficking to the apoplast, indicating that its membrane translocation is mechanistically coupled to LLG1 interaction. This pH-dependent modulation of protein-protein interactions provides a plausible mechanism by which ABP1 transitions from a trafficking-associated state to a signaling-competent state at the cell surface. Notably, while LLG1 has been well characterized as a co-receptor of FER that mediates RALF peptide perception and subsequent extracellular alkalinization (Haruta et al., 2014; Xiao et al., 2019), this study uncovers its novel function in ABP1 trafficking. This finding reveals a novel functional divergence for LLG1, demonstrating its capacity to operate autonomously from the canonical FER signaling pathway.

References

Amali, A.J., Awwad, N.H., Rana, R.K., and Patra, D. (2011). Nanoparticle assembled microcapsules for application as pH and ammonia sensor. Anal. Chim. Acta *708*, 75-83.

https://doi.org/10.1016/j.aca.2011.10.001.

Aryal, B., Jonsson, K., Baral, A., Sancho-Andres, G., Routier-Kierzkowska, A. L., Kierzkowski, D., and Bhalerao, R. P. (2020). Interplay between Cell Wall and Auxin Mediates the Control of Differential Cell Elongation during Apical Hook Development. Curr. Biol. *30*, 1733-1739. https://doi.org/10.1016/j.cub.2020.02.055.

Bellstaedt, J., Trenner, J., Lippmann, R., Poeschl, Y., Zhang, X., Friml, J., Quint, M., and Delker, C. (2019). A Mobile Auxin Signal Connects Temperature Sensing in Cotyledons with Growth Responses in Hypocotyls. Plant Physiol. *180*, 757-766. https://doi.org/10.1104/pp.18.01377.

Li, C., Yeh, F. L., Cheung, A. Y., Duan, Q., Kita, D., Liu, M. C., Maman, J., Luu, E. J., Wu, B. W., Gates, L., et al. (2015). Glycosylphosphatidylinositol-anchored proteins as chaperones and co-receptors for FERONIA receptor kinase signaling in Arabidopsis. eLife *4*, e06587. https://doi.org/10.7554/eLife.06587.

Chen, L., Tong, J., Xiao, L., Ruan, Y., Liu, J., Zeng, M., Huang, H., Wang, J.W., and Xu, L. (2016). YUCCA-mediated auxin biogenesis is required for cell fate transition occurring during de novo root organogenesis in Arabidopsis. J. Exp. Bot. *67*, 4273-4284. https://doi.org/10.1093/jxb/erw213.

Chen, R., Sun, P., Zhong, G., Wang, W., and Tang, D. (2022). The RECEPTOR-LIKE PROTEIN53 immune complex associates with LLG1 to positively regulate plant immunity. J. Integr. Plant Biol. 64, 1833-1846. https://doi.org/10.1111/jipb.13327.

Dahlke, R.I., Luthen, H., and Steffens, B. (2009). The auxin-binding pocket of auxin-binding protein 1 comprises the highly conserved boxes a and c. Planta *230*, 917-924. https://doi.org/10.1007/s00425-009-0995-2.

Dharmasiri, N., Dharmasiri, S., and Estelle, M. (2005). The F-box protein TIR1 is an auxin receptor. Nature *435*, 441-445. https://doi.org/10.1038/nature03542.

Dubey, S.M., Han, S., Stutzman, N., Prigge, M.J., Medvecka, E., Platre, M.P., Busch, W., Fendrych, M., and Estelle, M. (2023). The AFB1 auxin receptor controls the cytoplasmic auxin response pathway in Arabidopsis thaliana. Mol. Plant *16*, 1120-1130. https://doi.org/10.1016/j.molp.2023.06.008.

Dubey, S.M., Serre, N.B.C., Oulehlová, D., Vittal, P., and Fendrych, M. (2021). No Time for Transcription—Rapid Auxin Responses in Plants. Cold Spring Harb. Perspect. Biol. *13*, a039891. https://doi.org/10.1101/cshperspect.a039891.

Eui-Jeon Woo, J.M., James Bauly, Jin-Gui Chen, Michael Venis, Richard M.Napier and Richard W.Pickersgill (2002). Crystal structure of auxin-binding protein 1 in complex with auxin. EMBO J. *21*, 2877-2885. https://doi.org/10.1093/emboj/cdf291.

Feng, H., Liu, C., Fu, R., Zhang, M., Li, H., Shen, L., Wei, Q., Sun, X., Xu, L., Ni, B., *et al.* (2019). LORELEI-LIKE GPI-ANCHORED PROTEINS 2/3 Regulate Pollen Tube Growth as Chaperones and Coreceptors for ANXUR/BUPS Receptor Kinases in Arabidopsis. Mol. Plant *12*, 1612-1623. https://doi.org/10.1016/j.molp.2019.09.004.

Fiedler, L. and Friml, J. (2023). Rapid auxin signaling: Unknowns old and new. Curr. Opin. Plant Biol. *75*, 102443. https://doi.org/10.1016/j.pbi.2023.102443.

Friml, J. (2022). Fourteen Stations of Auxin. Cold Spring Harb. Perspect. Biol. *14*, a039859. https://doi.org/10.1101/cshperspect.a039859.

Friml, J., Gallei, M., Gelová, Z., Johnson, A., Mazur, E., Monzer, A., Rodriguez, L., Roosjen, M., Verstraeten, I., Živanović, B. D., et al. (2022). ABP1-TMK auxin perception for global phosphorylation

and auxin canalization. Nature *609*, 575-581. https://doi.org/10.1038/s41586-022-05187-x.

Fuglsang, A.T., Kristensen, A., Cuin, T.A., Schulze, W.X., Persson, J., Thuesen, K.H., Ytting, C.K., Oehlenschlaeger, C.B., Mahmood, K., Sondergaard, T.E., et al. (2014). Receptor kinase-mediated control of primary active proton pumping at the plasma membrane. Plant J. *80*, 951-964. https://doi.org/10.1111/tpj.12680.

Fujita, M. and Kinoshita, T. (2012). GPI-anchor remodeling: potential functions of GPI-anchors in intracellular trafficking and membrane dynamics. Biochim. Biophys. Acta *1821*, 1050-1058. https://doi.org/10.1016/j.bbalip.2012.01.004.

Fujita, M., Watanabe, R., Jaensch, N., Romanova-Michaelides, M., Satoh, T., Kato, M., Riezman, H., Yamaguchi, Y., Maeda, Y., and Kinoshita, T. (2011). Sorting of GPI-anchored proteins into ER exit sites by p24 proteins is dependent on remodeled GPI. J. Cell Biol. *194*, 61-75. https://doi.org/10.1083/jcb.201012074.

Gao, Y., Zhang, Y., Zhang, D., Dai, X., Estelle, M., and Zhao, Y. (2015). Auxin binding protein 1 (ABP1) is not required for either auxin signaling or Arabidopsis development. Proc. Natl. Acad. Sci. U.S.A. *112*, 2275-2280. https://doi.org/10.1073/pnas.1500365112.

Gelová, Z., Gallei, M., Pernisová, M., Brunoud, G., Zhang, X., Glanc, M., Li, L., Michalko, J., Pavlovičová, Z., Verstraeten, I., et al. (2021). Developmental roles of Auxin Binding Protein 1 in Arabidopsis thaliana. Plant Sci. *303*, 110750. https://doi.org/10.1016/j.plantsci.2020.110750.

Guillaume Alain Castillon, L.M., and Reika Watanabe (2013). Apical sorting of lysoGPI-anchored proteins occurs independent of association with detergent-resistant membranes but dependent on their N-glycosylation. Molecular Biology of the Cell *24*, 2021-2033. https://doi.org/10.1091/mbc.E13-03-0160.

Haruta, M., Sabat, G., Stecker, K., Minkoff, B. B. and Sussman, M. R. (2014). A peptide hormone and its receptor protein kinase regulate plant cell expansion. Science *343*, 408-411. https://doi.org/10.1126/science.1244454.

Horvath, A., Sutterlin, C., Manning-Krieg, U., Movva, N. R. and Riezman, H. (1994). Ceramide synthesis enhances transport of GPI-anchored proteins to the Golgi apparatus in yeast. EMBO J. *13*, 3687-3695. https://doi.org/10.1002/j.1460-2075.1994.tb06678.x.

Hu, T., Yin, S., Sun, J., Linghu, Y., Ma, J., Pan, J., and Wang, C. (2021). Clathrin light chains regulate hypocotyl elongation by affecting the polarization of the auxin transporter PIN3 in Arabidopsis. J. Integr. Plant Biol. *63*, 1922-1936. https://doi.org/10.1111/jipb.13171.

Huang, S., Yang, C. and Li, L. (2022). Unraveling the Dynamic Integration of Auxin, Brassinosteroid and Gibberellin in Early Shade-Induced Hypocotyl Elongation. Phenomics *2*, 119-129. https://doi.org/10.1007/s43657-022-00044-3.

Huang, Y., Yin, C., Liu, J., Feng, B., Ge, D., Kong, L., Ortiz-Morea, F. A., Richter, J., Hauser, M. T., Wang, W. M., et al. (2020). A trimeric CrRLK1L-LLG1 complex genetically modulates SUMM2-mediated autoimmunity. Nat. Commun. *11*, 4859. https://doi.org/10.1038/s41467-020-18600-8.

Jones, A. M. and Herman, E. M. (1993). KDEL-Containing Auxin-Binding Protein Is Secreted to the Plasma Membrane and Cell Wall. Plant Physiol. *101*, 595-606. https://doi.org/10.1104/pp.101.2.595.

Kakei, Y., Yamazaki, C., Suzuki, M., Nakamura, A., Sato, A., Ishida, Y., Kikuchi, R., Higashi, S., Kokudo, Y., Ishii, T., et al. (2015). Small-molecule auxin inhibitors that target YUCCA are powerful tools for studying auxin function. Plant J. *84*, 827-837. https://doi.org/10.1111/tpj.13032.

Kepinski, S., and Leyser, O. (2005). The Arabidopsis F-box protein TIR1 is an auxin receptor. Nature *435*, 446-451. https://doi.org/10.1038/nature03542.

Kuhn, A., Roosjen, M., Mutte, S., Dubey, S.M., Carrillo Carrasco, V.P., Boeren, S., Monzer, A., Koehorst, J., Kohchi, T., Nishihama, R., et al. (2024). RAF-like protein kinases mediate a deeply conserved, rapid auxin response. Cell *187*, 130-148. https://doi.org/10.1016/j.cell.2023.11.021.

Lavy, M. and Estelle, M. (2016). Mechanisms of auxin signaling. Development *143*, 3226-3229. https://doi.org/10.1242/dev.131870.

Lescot, M., Déhais, P., Thijs, G., Marchal, K., Moreau, Y., Van de Peer, Y., Rouzé, P., and Rombauts, S. (2002). PlantCARE, a database of plant cis-acting regulatory elements and a portal to tools for in silico analysis of promoter sequences. Nucleic Acids Res. *30*, 325-327. https://doi.org/10.1093/nar/30.1.325.

Lin, W., Zhou, X., Tang, W., Takahashi, K., Pan, X., Dai, J., Ren, H., Zhu, X., Pan, S., Zheng, H., et al. (2021). TMK-based cell-surface auxin signalling activates cell-wall acidification. Nature *599*, 278-282. https://doi.org/10.1038/s41586-021-03976-4.

Liu, Z., Chu, X., Ren, W., Cheng, L., Liu, C., Wang, C., Gao, S., Dai, S., and Li, C. (2025). PCP-B peptides and CrRLK1L receptor kinases control pollination via pH gating of aquaporins in Arabidopsis. Dev. Cell *60*, 1336-1347. https://doi.org/10.1016/j.devcel.2024.12.026.

Löbler, M. and Klämbt, D. (1985). Auxin-binding protein from coleoptile membranes of corn (Zea mays L.). I. Purification by immunological methods and characterization. J. Biol. Chem. *260*, 9848-9853. https://doi.org/10.1016/s0021-9258(17)39314-6.

Lu, B., Wang, S., Feng, H., Wang, J., Zhang, K., Li, Y., Wu, P., Zhang, M., Xia, Y., Peng, C., et al. (2024). FERONIA-mediated TIR1/AFB2 oxidation stimulates auxin signaling in Arabidopsis. Mol. Plant *17*, 772-787. https://doi.org/10.1016/j.molp.2024.04.002.

Luschnig, C., and Friml, J. (2024). Over 25 years of decrypting PIN-mediated plant development. Nat. Commun. *15*, 9904. https://doi.org/10.1038/s41467-024-54240-y.

Maeda, Y. and Kinoshita, T. (2011). Structural remodeling, trafficking and functions of glycosylphosphatidylinositol-anchored proteins. Prog. Lipid Res. *50*, 411-424. https://doi.org/10.1016/j.plipres.2011.05.002.

Mano, Y. and Nemoto, K. (2012). The pathway of auxin biosynthesis in plants. J. Exp. Bot. *63*, 2853-2872. https://doi.org/10.1093/jxb/ers091.

Muñiz, M. and Riezman, H. (2016). Trafficking of glycosylphosphatidylinositol anchored proteins from the endoplasmic reticulum to the cell surface. J. Lipid Res. *57*, 352-360. https://doi.org/10.1194/jlr.R062760.

Napier, R. (2021). The Story of Auxin-Binding Protein 1 (ABP1). Cold Spring Harb. Perspect. Biol. *13*, a039909. https://doi.org/10.1101/cshperspect.a039909.

Palazzo, F. C., Sitia, R. and Tempio, T. (2022). Selective Secretion of KDEL-Bearing Proteins: Mechanisms and Functions. Front. Cell Dev. Biol. *10*, 967875. https://doi.org/10.3389/fcell.2022.967875.

Qiujing Shena, G. B., Huairong Pan, Silke Robatzek, and Dingzhong Tang (2017). Arabidopsis glycosylphosphatidylinositol-anchored protein LLG1 associates with and modulates FLS2 to regulate innate immunity. Proc. Natl. Acad. Sci. U.S.A. *114*, 5749-5754. https://doi.org/10.1073/pnas.1614468114.

R. Hertel, K.-S. T., and V. E. A. Russo (1972). In-vitro Auxin Binding to Particulate Cell Fractions from

Corn Coleoptiles. Planta *107*, 325-340. https://doi.org/10.1007/BF00386394.

Rodriguez, L., Fiedler, L., Zou, M., Giannini, C., Monzer, A., Vladimirtsev, D., Randuch, M., Yu, Y., Gelová, Z., Verstraeten, I., et al. (2025). ABP1/ABL3-TMK1 cell-surface auxin signaling targets PIN2-mediated auxin fluxes for root gravitropism. Cell *188*, 6138-6150. https://doi.org/10.1016/j.cell.2025.08.026.

Satpute-Krishnan, P., Ajinkya, M., Bhat, S., Itakura, E., Hegde, Ramanujan S., and Lippincott-Schwartz, J. (2014). ER Stress-Induced Clearance of Misfolded GPI-Anchored Proteins via the Secretory Pathway. Cell *158*, 522-533. https://doi.org/10.1016/j.cell.2014.06.026.

Serre, N.B.C., Kralik, D., Yun, P., Slouka, Z., Shabala, S., and Fendrych, M. (2021). AFB1 controls rapid auxin signalling through membrane depolarization in Arabidopsis thaliana root. Nat. Plants *7*, 1229-1238. https://doi.org/10.1038/s414.

Shimomura, S. (2006). Identification of a glycosylphosphatidylinositol-anchored plasma membrane protein interacting with the C-terminus of auxin-binding protein 1: a photoaffinity crosslinking study. Plant Mol. Biol. *60*, 663-677. https://doi.org/10.1007/s11103-005-5471-1.

Shoji SHIMOMURA, T.S.F., and Toshio FUKUI (1986). Purifcation and Properties of an Auxin-Binding Proteinfrom Maize Shoot Membranes. J. Biochem. *99*, 1513-1524. https://doi.org/10.1093/oxfordjournals.jbchem.a135621.

Klode, M., Dahlke, R. I., Sauter, M., and Steffens, B. (2011). Expression and Subcellular Localization of Arabidopsis thaliana Auxin-Binding Protein 1 (ABP1). J. Plant Growth Regul. *30*, 416-424. https://doi.org/10.1007/s00344-011-9203-2.

Tian, H., Klämbt, D., and Jones, A.M. (1995). Auxin-binding Protein 1 Does Not Bind Auxin within the Endoplasmic Reticulum Despite This Being the Predominant Subcellular Location for This Hormone Receptor. J. Biol. Chem. *270*, 26962-26969. https://doi.org/10.1074/jbc.270.45.26962.

Vanneste, S., and Friml, J. (2009). Auxin: a trigger for change in plant development. Cell *136*, 1005-1016. https://doi.org/10.1016/j.cell.2009.03.001.

Xiao, Y., Stegmann, M., Han, Z., DeFalco, T.A., Parys, K., Xu, L., Belkhadir, Y., Zipfel, C., and Chai, J. (2019). Mechanisms of RALF peptide perception by a heterotypic receptor complex. Nature *572*, 270-274. https://doi.org/10.1038/s41586-019-1409-7.

Xu, T., Wen, M., Nagawa, S., Fu, Y., Chen, J.G., Wu, M.J., Perrot-Rechenmann, C., Friml, J., Jones, A.M., and Yang, Z. (2010). Cell surface- and rho GTPase-based auxin signaling controls cellular interdigitation in Arabidopsis. Cell *143*, 99-110. https://doi.org/10.1016/j.cell.2010.09.003.

Xu, Z., Gao, Y., Gao, C., Mei, J., Wang, S., Ma, J., Yang, H., Cao, S., Wang, Y., Zhang, F.*, et al.* (2022). Glycosylphosphatidylinositol anchor lipid remodeling directs proteins to the plasma membrane and governs cell wall mechanics. Plant Cell *34*, 4778-4794. https://doi.org/10.1093/plcell/koac257.

Yang, Z., Xia, J., Hong, J., Zhang, C., Wei, H., Ying, W., Sun, C., Sun, L., Mao, Y., Gao, Y.*,* et al. (2022). Structural insights into auxin recognition and efflux by Arabidopsis PIN1. Nature *609*, 611-615. https://doi.org/10.1038/s41586-022-05143-9.

Yu, Y., Tang, W., Lin, W., Li, W., Zhou, X., Li, Y., Chen, R., Zheng, R., Qin, G., Cao, W.*,* et al. (2023). ABLs and TMKs are co-receptors for extracellular auxin. Cell *186*, 5457-5471. https://doi.org/10.1016/j.cell.2023.10.017.

Zavaliev, R., Dong, X., and Epel, B.L. (2016). Glycosylphosphatidylinositol (GPI) modification serves as a primary plasmodesmal targeting signal. Plant physiol. *172*, 1061-1073. https://doi.org/10.1104/pp.

546 16.01026.
547 Zhang, Q., and Fujita, M. (2024). Why nature evolved GPI-anchored proteins: unique structure
548 characteristics enable versatile cell surface functions. Glycobiology *34*, cwae089. https://doi.org/10.109
549 3/glycob/cwae089.
550

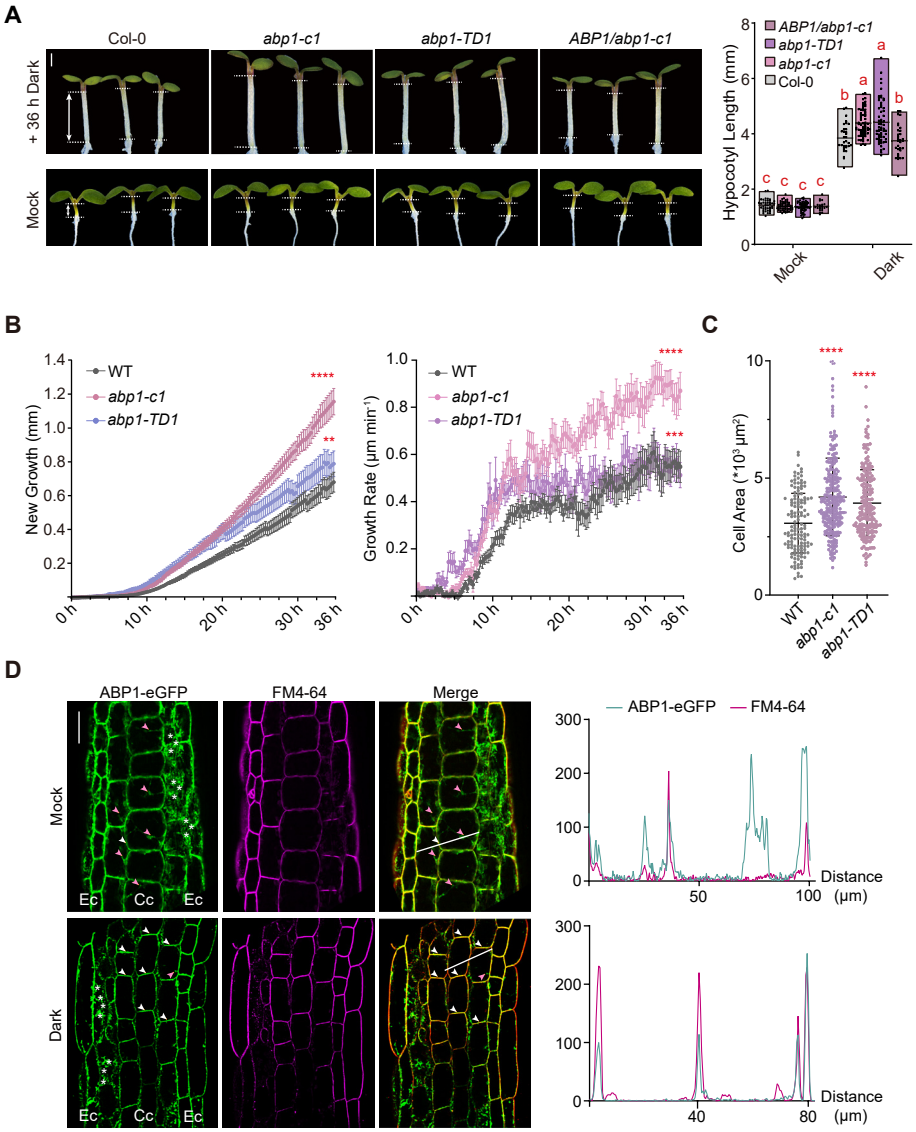

Figure 1. ABP1 participates in dark-induced hypocotyl elongation in *Arabidopsis*

(A) Phenotype analysis and quantification of hypocotyl length in 4-day-old *abp1-c1*, *abp1-TD1 and pABP1:ABP1-eGFP/abp1-c1* seedlings subjected to mock or dark treatment for 36 h. $n \geq 21$ hypocotyls. Scale bar, 2 mm.

(B) Time-lapse analysis of hypocotyl new growth and growth rate in 4-day-old WT, *abp1-c1* and *abp1-TD1* seedlings during continuous dark treatment for 36 h. Images were captured every 15 min. $n \geq 28$ hypocotyls.

(C) Quantification of hypocotyl cell areas in 4-day-old WT, *abp1-c1* and *abp1-TD1* seedlings subjected to dark treatment for 36 h. $n \geq 135$ cells from 24–39 hypocotyls.

(D) Confocal microscopy imaging and fluorescence plot profiling of ABP1-eGFP in hypocotyl cortical cells of seedlings subjected to dark treatment for 18 h. Ec, epidermal cell; Cc, cortex cell. stars lable the unfocused areas. White line is used for fluorescence intensity measurement; FM4-64 labels the PM; white arrowheads indicate the colocalized signal; pink arrowheads indicate the non-colocalized signal; Scale bar, 50 μm.

In (A–C), data are presented as mean ± SD. Significant differences were determined using two-way ANOVA. Different lowercase letters indicate significant differences at $P < 0.05$ (A). Significant differences were determined using Student's *t*-test (B–C). $^{**}P < 0.01$, $^{***}P < 0.001$, $^{****}P < 0.0001$.

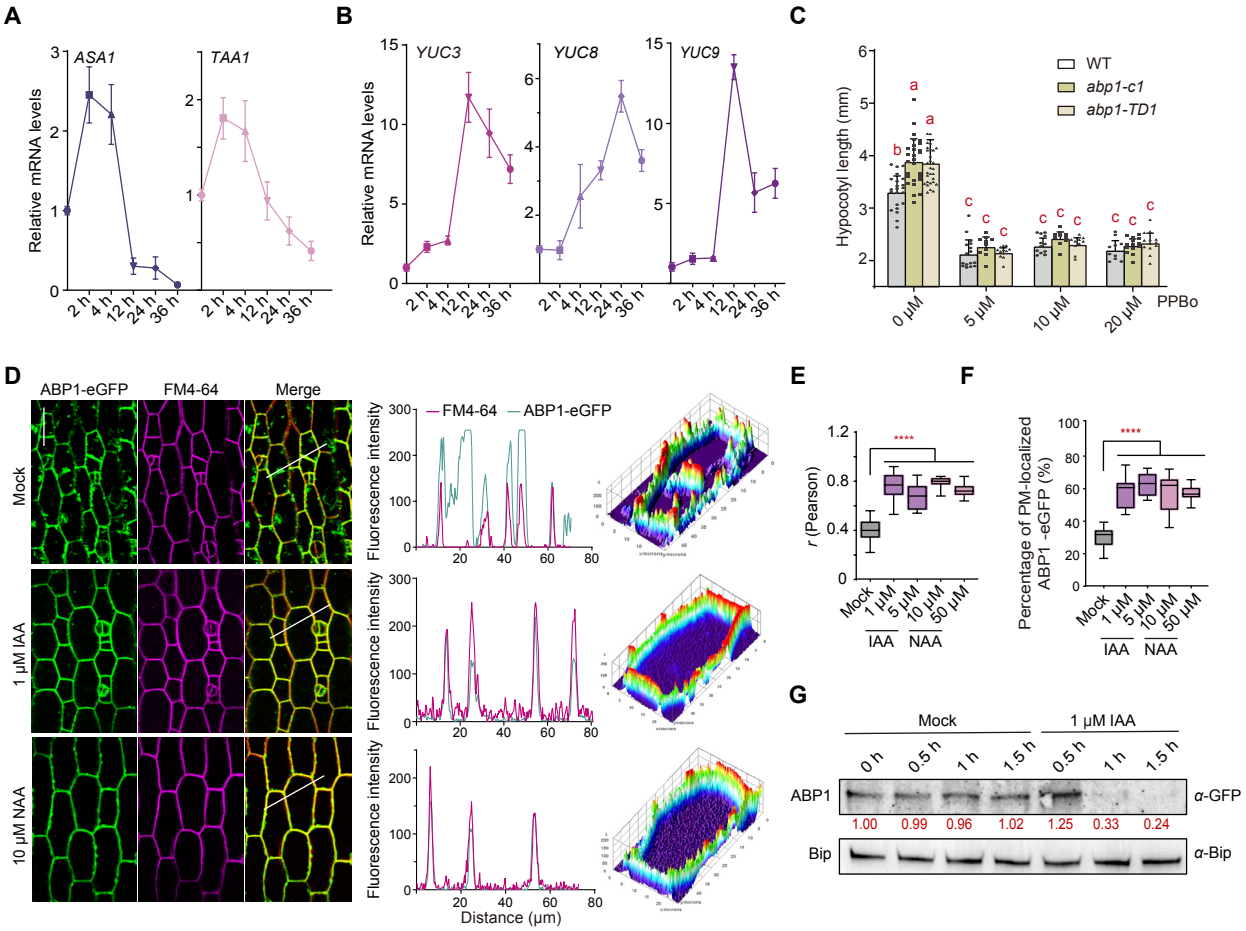

Figure 2. Dark treatment induces ABP1 trafficking through auxin biosynthesis in hypocotyl

(A–B) RT-qPCR analysis of *ASA1*, *TAA1*, *YUC3*, *YUC8* and *YUC9* in aboveground part of 4-day-old seedlings subjected to darkness for 0, 2, 4, 12, 24 or 36 h. Transcript levels were expressed as fold change relative to 0 h (set to 1).

(C) Quantification of hypocotyl length in 4-day-old light-grown *abp1-c1* and *abp1-TD1* seedlings followed by 36 h co-treatment of dark and auxin inhibitor targeting *YUCCA*s, PPBo. $n \geq 10$ hypocotyls.

(D) Confocal microscopy images (left), fluorescence plot profiles (middle), and 3D surface plots (right) of hypocotyl epidermal cells in 4-day-old seedlings treated with/without IAA or NAA for 1 h. FM4-64 labels the PM. White lines indicate fluorescence measurement regions. Scale bar, 20 μm.

(E) Pearson's coefficient of ABP1-eGFP and FM4-64 colocalization after IAA or NAA treatment for 1 h. $n \geq 13$ cells from 3–4 hypocotyls. (*r*), Pearson's colocalization coefficient.

(F) The percentage of PM-localized ABP1-eGFP in hypocotyl epidermal cells of 4-day-old seedlings with/without IAA or NAA treatments for 1 h. $n \geq 15$ cells from 3–4 hypocotyls.

(G) Western blot analysis of ABP1-eGFP protein levels following IAA treatment in ER fraction. *α*-Bip serves as ER marker. Red numbers indicate relative ABP1-eGFP protein levels at each time point relative to untreated control.

In (C, E–F), data are presented as mean ± SD. Significant differences were determined using two-way ANOVA (C). Different lowercase letters indicate significant differences at $P < 0.05$. Significant differences were determined using Student's *t*-test (E–F). ****$P < 0.0001$.

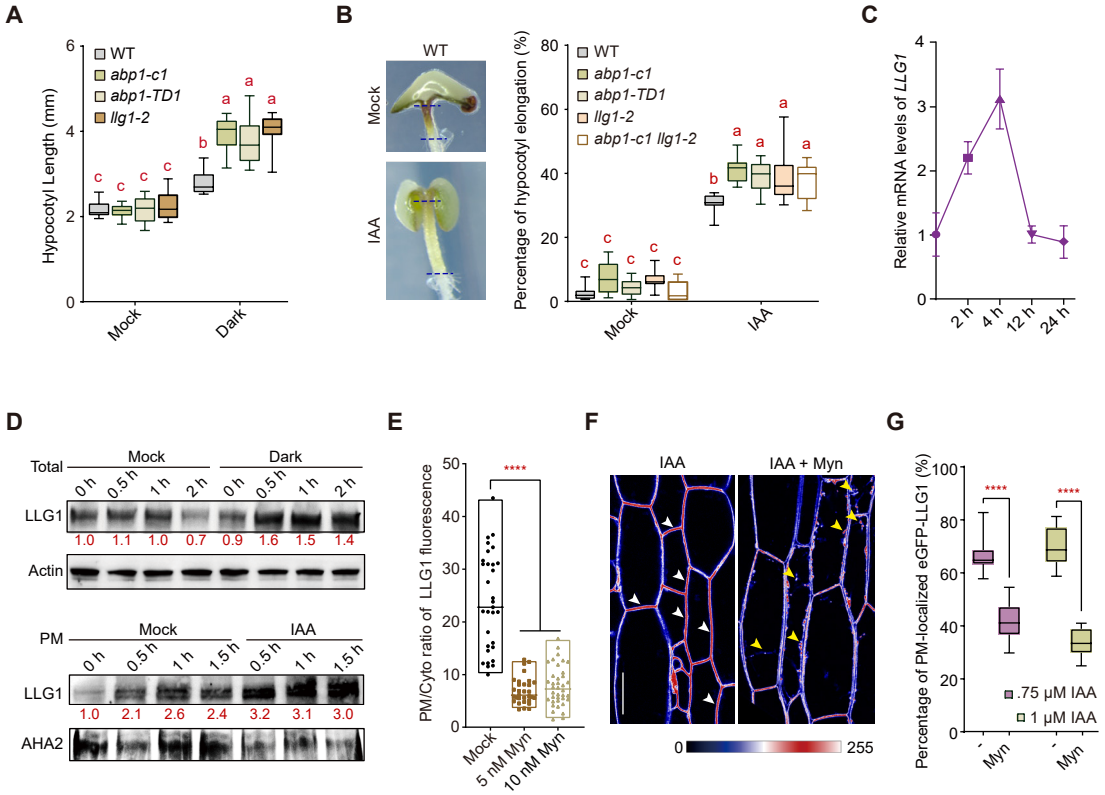

Figure 3. Dark-induced auxin stimulates the transcriptional expression of *LLG1*

(A) Quantification of hypocotyl length in 4-day-old WT, *abp1-c1*, *abp1-TD1 and llg1-2* seedlings subjected to dark treatment for 36 h. $n \geq 10$ hypocotyls.

(B) Schematic illustration of the lanolin paste application and representative phenotypes of WT seedlings with or without 1 mM IAA treatment applied to the cotyledons. Quantification of hypocotyl elongation in 4-day-old light-grown WT, *abp1-c1*, *abp1-TD1*, *llg1-2* and *abp1-c1 llg1-2* seedlings with or without IAA treatment. $n \geq 9$ hypocotyls.

(C) RT-qPCR analysis of *LLG1* in aboveground tissues of 4-day-old seedlings subjected to darkness for 0–24 h. Transcription levels were indicated as fold change relative to 0 h (set to 1).

(D) Western blot analysis of eGFP-LLG1 protein levels under darkness and IAA treatment. Total protein levels of eGFP-LLG1 in 4-day-old seedlings subjected to darkness for the indicated periods are shown (top). Plasma membrane (PM) fractions were isolated and analyzed for eGFP-LLG1 protein levels after IAA treatment for the indicated periods (bottom), with α-AHA2 used as a PM marker. Numbers in red indicate the relative protein amount of eGFP-LLG1 at each time point compared with the non-treated sample.

(E) Quantification of PM/cytoplasm LLG1 fluorescence signal ratio of root hair in 3.5-day-old *pLLG1:sp-eGFP-LLG1* transgenic seedlings with/without Myn treatment.

(F) Confocal microscopy imaging of hypocotyl epidermal cells in 4-day-old seedlings treated with IAA alone or Myn co-treatment (pseudo-colored with UnionJack LUT). Scale bar, 20 μm.

(G) The percentage of PM-localized eGFP-LLG1 in hypocotyl epidermal cells of 4-day-old seedlings treated with IAA alone or Myn co-treatment.

In (A, B E–G), data are presented as mean ± SD. Significant differences were determined using two-way ANOVA (A, B). Different lowercase letters indicate significant differences at $P < 0.01$. Significant differences were determined using Student's *t*-test (E–G). ****$P < 0.0001$.

See also, Figure S3.

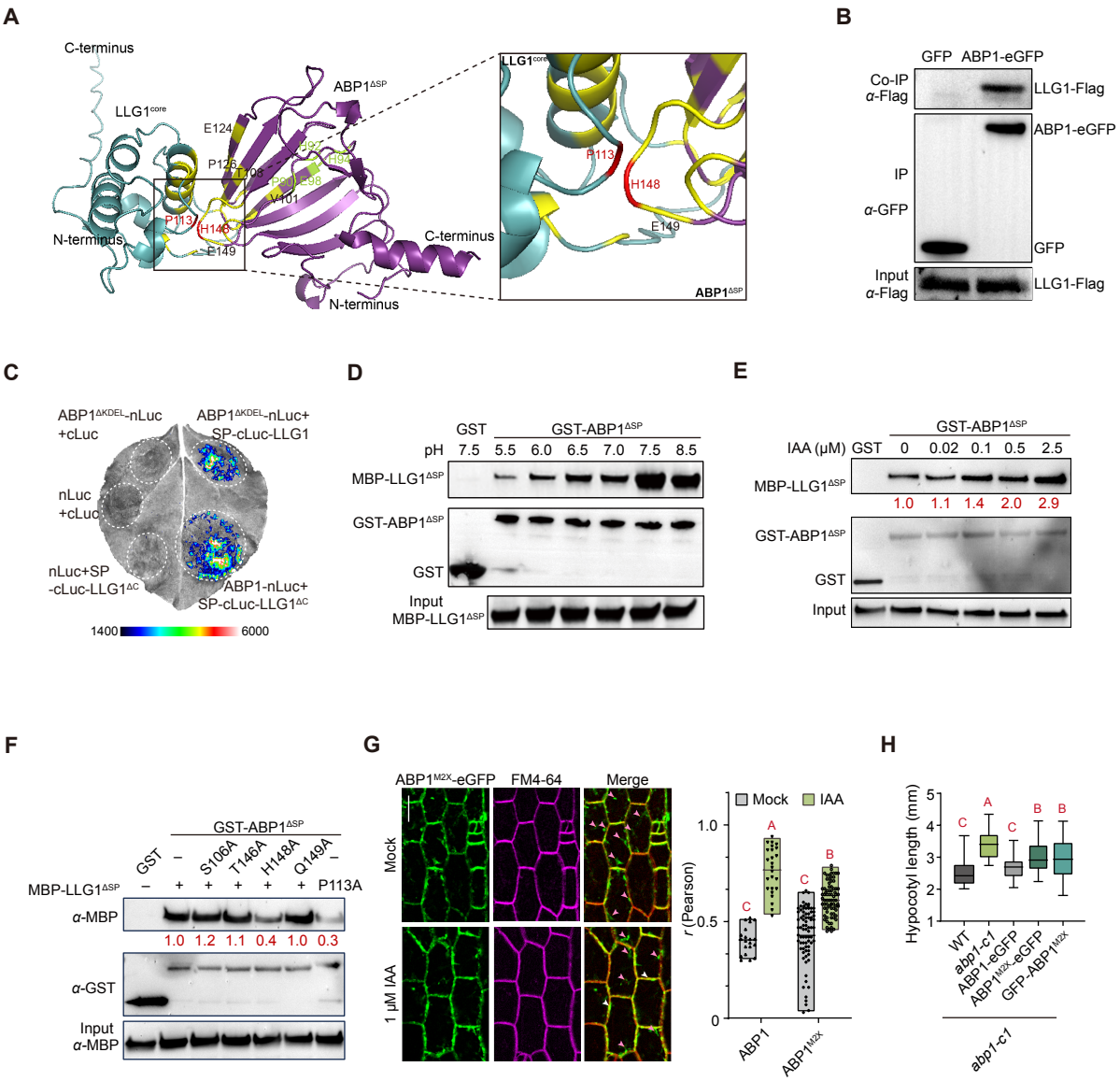

Figure 4. Auxin stimulates the LLG1 interaction with ABP1 in a pH-dependent manner

(A) AlphaFold3 protein interaction analysis of ABP1$^{\Delta SP}$ and LLG1^{core}. Yellow highlights the predicted ABP1$^{\Delta SP}$–LLG1^{core} interaction interface. The right panel shows an enlarged view of the interface, with LLG1^{core} shown in blue and ABP1$^{\Delta SP}$ shown in purple. The yellow region indicates the interaction interface and marks the 6 amino acid residues of ABP1$^{\Delta SP}$ involved in the predicted interaction. The green region highlights four key amino acid residues constituting the NAA-binding pocket. The orange region highlights W151, a key amino acid involved in the conformation of the C-terminus after binding of IAA.

(B) Co-IP of ABP1-eGFP and LLG1-Flag from the *pABP1:ABP1-eGFP pLLG1:sp-mCherry-LLG1-Flag* transgenic plants using anti-Flag antibody. ABP1-eGFP was detected by anti-GFP antibody.

(C) Luciferase complementation assay showing the interaction between ABP1$^{\Delta KDEL}$ and LLG1 or ABP1 and LLG1$^{\Delta C}$.

(D) Pull-down assay showing ABP1$^{\Delta SP}$–LLG1$^{\Delta SP}$ interaction under pH 5.5–pH 8.5.

(E) Pull-down assay showing ABP1$^{\Delta SP}$–LLG1$^{\Delta SP}$ interaction after IAA treatment under pH 7.5.

(F) Pull-down assay demonstrating interactions between: GST-ABP1^{Mut} (S106A, T146A, H148A, Q149A) and MBP-LLG1$^{\Delta SP}$ (Lane 3–6), GST-ABP1$^{\Delta SP}$ and MBP-LLG1^{P113A} (Lane 7) under pH 7.5.

(G) Fluorescence imaging and pearson's coefficient of hypocotyl epidermal cells in 4-day-old *pABP1:ABP1^{M2X}-eGFP/abp1-c1* seedlings treated with/without IAA for 1 h. White arrowheads indicate the colocalization signal. Pink arrowheads indicate the non-colocalization signal. (*r*), Pearson's colocalization coefficient. Scale bar, 40 μm.

(H) Quantification of hypocotyl length in 4-day-old WT, *abp1-c1*, *pABP1:ABP1-eGFP/abp1-c1*, *pABP1:GFP-ABP1^{M2X}/abp1-c1* and *pABP1:ABP1^{M2X}-eGFP/abp1-c1* transgenic plants subjected to darkness for 36 h. n ≥ 45 hypocotyls.

In (G–H), data are presented as mean ± SD. Significant differences were determined using one-way ANOVA. Different uppercase letters indicate significant differences at $P < 0.01$.

See also, Figure S4.

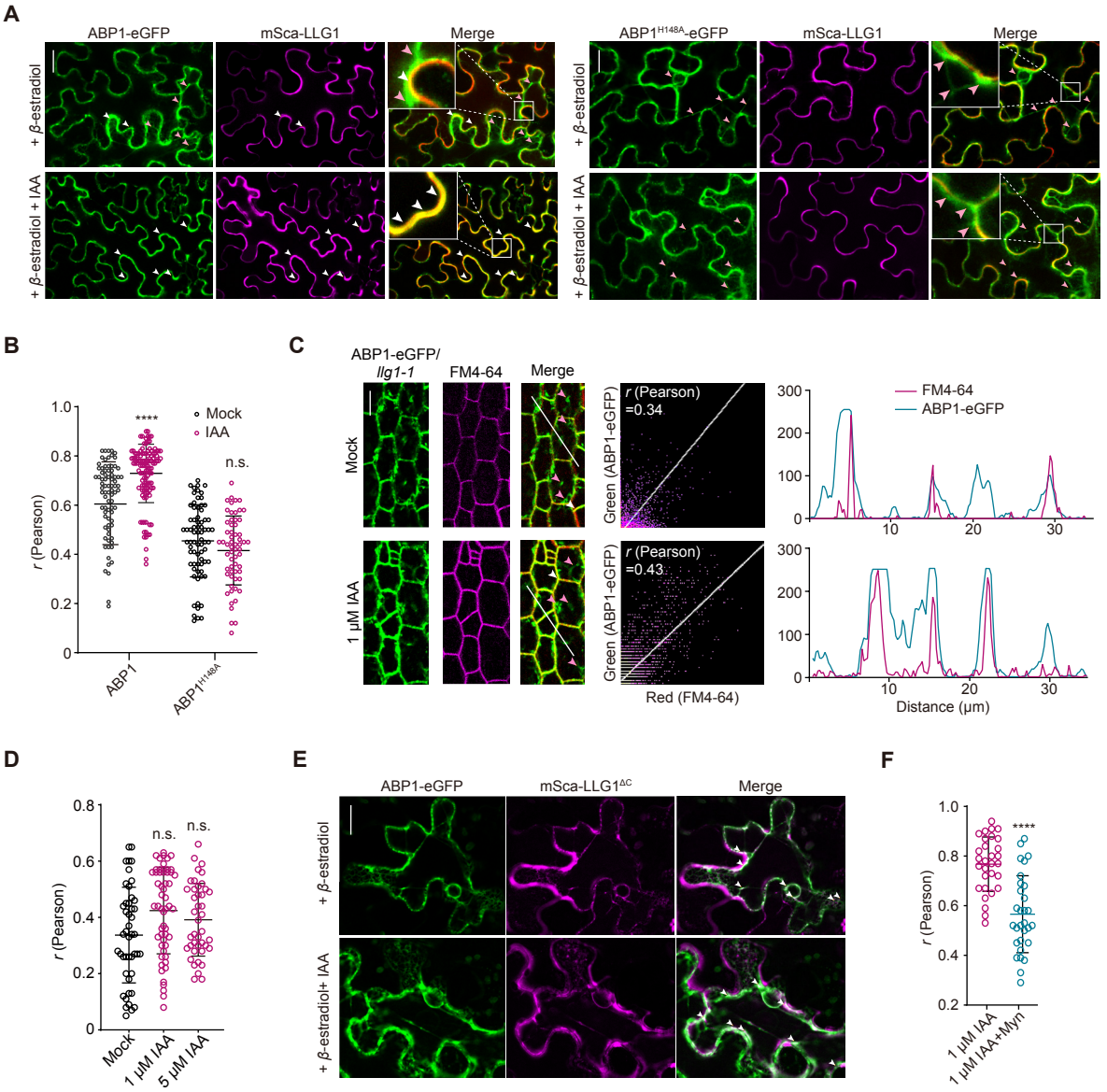

Figure 5. **LLG1 facilitates auxin-induced ABP1 trafficking from ER to PM**

(A–B) Fluorescence imaging and pearson's coefficient of ABP1 (or ABP1^{H148A}) and LLG1 in tobacco leaves. *pABP1:ABP1-eGFP* and *pER8:mSca-LLG1* were transformed to *N. benthamiana* leaves and treated with *β*-estradiol for 24 h and 1 μM IAA treatment for 35 min. Pink arrowheads indicate the ER regions. White arrowheads indicate the regions of colocalization. $n \geq 61$ cells.

(C) Confocal microscopy imaging (left), scatterplot analysis with Pearson's colocalization coefficient (middle) and fluorescence plot profiles (right) of ABP1-eGFP in *llg1-1* background in hypocotyl epidermal cells of 4-day-old seedlings with/without IAA treatment for 1 h. FM4-64 staining indicates the PM, white arrowheads indicate the colocalized signal; pink arrowheads indicate the non-colocalized signal.. White lines are used for fluorescence intensity measurement.

(D) Pearson's coefficient showing the colocalization of FM4-64 and ABP1-eGFP in *llg1-1* background after IAA treatment for 1 h. $n \geq 42$ cells from 15 hypocotyls.

(E) Fluorescence imaging of ABP1-eGFP with mSca-LLG1$^{\Delta C}$ co-expression in *N. benthamiana* leaves. *pABP1::ABP1-eGFP* and *pER8::mSca-LLG1$^{\Delta C}$* in *N. benthamiana* leaves were treated with *β*-estradiol for 24 h and 1 μM IAA treatment for 35 min. White arrowheads indicate the regions of colocalization.

(F) Pearson's coefficient of ABP1-eGFP and FM4-64 colocalization treated with IAA alone or Myn co-treatment. $n = 30$ cells.

Scale bars, 20 μm (A, E) and 10 μm (C). (*r*), Pearson's colocalization coefficient. In (B, D, F), data are presented as mean ± SD. Significant differences were determined using Student's *t*-test. n.s., not significant. ****$P < 0.0001$.

See also, Figure S5.

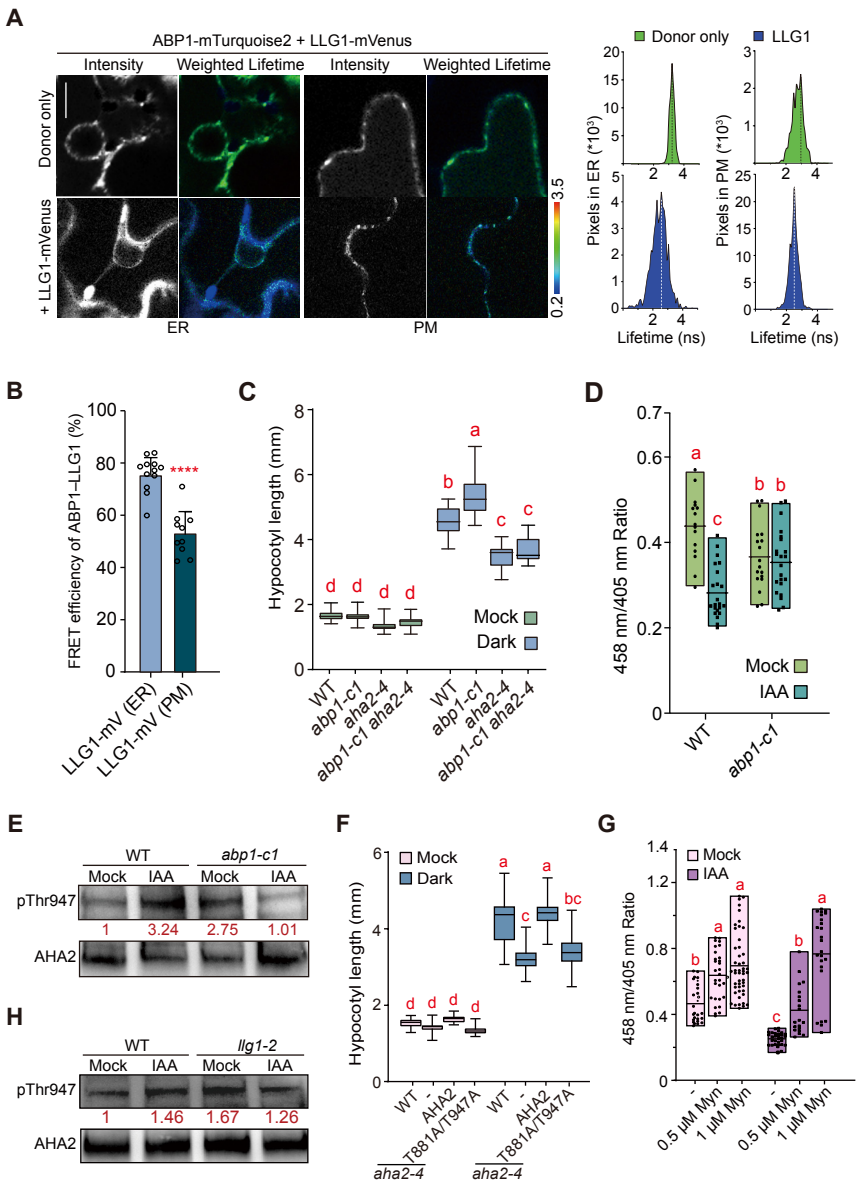

Figure 6. ABP1 regulates the AHA1/2-mediated dark-induced apoplast acidification and hypocotyl elongation

(A) Representative FRET-FLIM images (left), lifetime histograms (right) of the ABP1–LLG1 interaction at ER and PM. Intensity-weighted lifetime images use rainbow LUT pseudo-colouring. Histogram dashed lines mark peak lifetime values. Scale bar, 10 μm.

(B) Quantification of FRET efficiency of the ABP1–LLG1 interaction at ER and PM. $n \geq 10$ cells.

(C) Quantification of hypocotyl length in WT, *abp1-c1*, *aha2-4* and *abp1-c1 aha2-4* seedlings subjected to darkness for 30 h. $n \geq 23$ seedlings.

(D) Relative quantification of HPTS-stained apoplastic pH in hypocotyl cortex cells in 4-day-old WT and *abp1-c1* seedlings after dark treatment for 18 h following 1 μM IAA treatment for 15 min. $n \geq 15$ cells.

(E) Western blot detection of phosphorylated AHA2 in WT and *abp1-c1* seedlings (anti-pThr947). AHA2 protein levels were determined using anti-AHA2 antibodies. Seedlings were subjected to darkness for 12 h followed by 1 μM IAA treatment for 10 min.

(F) Quantification of hypocotyl length in *aha2-4*, *pAHA2::AHA2/aha2-4* and *pAHA2::AHA2*$^{T881A/T947A}$*/aha2-4* seedlings subjected to darkness for 30 h. $n \geq 20$ seedlings.

(G) Relative quantification of HPTS-stained pH in the apoplast of hypocotyl cortical cells in 3-day-old WT seedlings treated with Myn for 1 d followed by 18 h dark treatment and then 1 μM IAA treatment for 15 min. $n \geq 22$ cells.

(H) Western blot detection of phosphorylated AHA2 in WT and *llg1-2* seedlings (anti-pThr947). AHA2 protein levels were determined using anti-AHA2 antibodies. Seedlings were subjected to darkness for 12 h followed by 1 μM IAA treatment for 10 min.

In (B–D, F–G), data are presented as mean ± SD. Significant differences were determined using Student's *t*-test (B) or two-way ANOVA (C–D, F–G). **** $P < 0.0001$. Different lowercase letters indicate significant differences at $P < 0.05$.

See also, Figures S6 and S7.

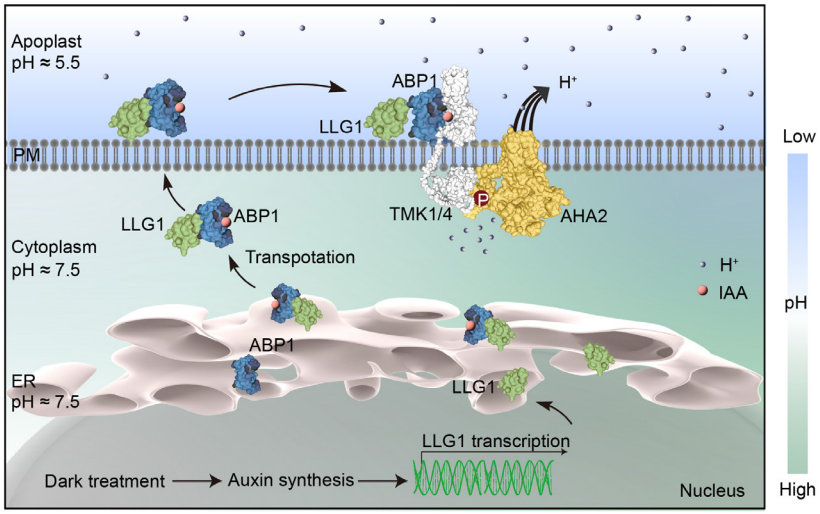

Figure 7. Model of dark/auxin-induced and LLG1-facilitated ABP1 trafficking in hypocotyl elongation

Dark treatment induces auxin biosynthesis and subsequently stimulates *LLG1* expression. Auxin enhanced LLG1 interaction with ABP1 in the ER and assists its trafficking through GPI-AP unique pathway. Upon reaching the PM, ABP1 dissociates from LLG1 under apoplastic acidic conditions and subsequently reassembled with the TMK receptor kinases to initiate proton ATPase-mediated signaling.

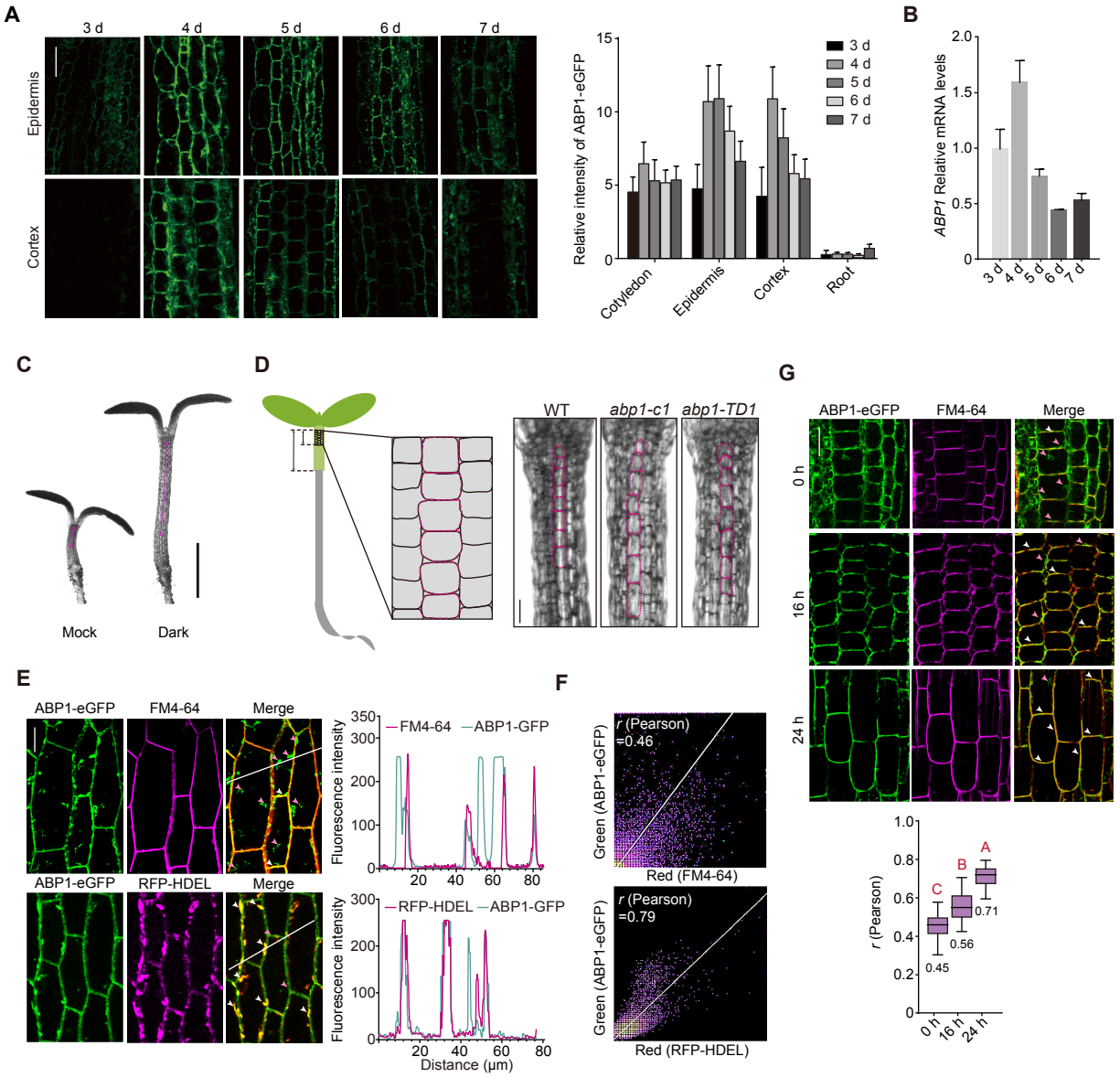

Figure S1. Auxin regulates hypocotyl elongation under dark condition, related to Figure 1

(A) Confocal microscopy imaging showing the expression of ABP1 in the hypocotyl of *pABP1::ABP1-eGFP* transgenic plants from day 3 to 7. Scale bar, 50 μm. Time-course analysis of the fluorescence intensity of ABP1-eGFP in cotyledon, hypocotyl epidermis, hypocotyl cortex and root. $n \geq 14$ seedlings.

(B) RT-qPCR analysis of *ABP1* expression in aboveground part of seedlings from day 3 to 7.

(C) Representative images of hypocotyl cell segment under double-point tracking. Red lines indicate the tracking region. Scale bar, 1 mm.

(D) Schematic representation of the hypocotyl cell region examined during this study. Phenotype of hypocotyl cell areas in 4-day-old WT, *abp1-c1* and *abp1-TD1* seedlings subjected to darkness for 30 h. Scale bar, 100 μm.

(E) Confocal microscopy imaging (left) and fluorescence plot profiles (right) of ABP1-eGFP in hypocotyl epidermal cells of 4-day-old seedlings. FM4-64 staining indicates the PM. RFP-HDEL indicates the ER. White arrowheads indicate the colocalization signal. Pink arrowheads indicate the non-colocalization signal. White lines are used for fluorescence intensity measurement. Scale bar, 20 μm.

(F) Scatterplot analysis of ABP1-eGFP colocalization with FM4-64 or RFP-HDEL in (E). (*r*), Pearson's colocalization coefficient.

(G) Confocal microscopy imaging of ABP1-eGFP in hypocotyl cortical cells of seedlings subjected to dark treatment for 16 or 24 h. Pearson's coefficient showing the colocalization of ABP1-eGFP and FM4-64-stained PM. (*r*), Pearson's colocalization coefficient. White arrowheads indicate the colocalized signal. Pink arrowheads indicate the non-colocalized signal. $n \geq 15$ cells from 3 hypocotyls. Scale bar, 40 μm. Data are presented as mean ± SD. Significant differences were determined using one-way ANOVA. Different uppercase letters indicate significant differences at $P < 0.01$.

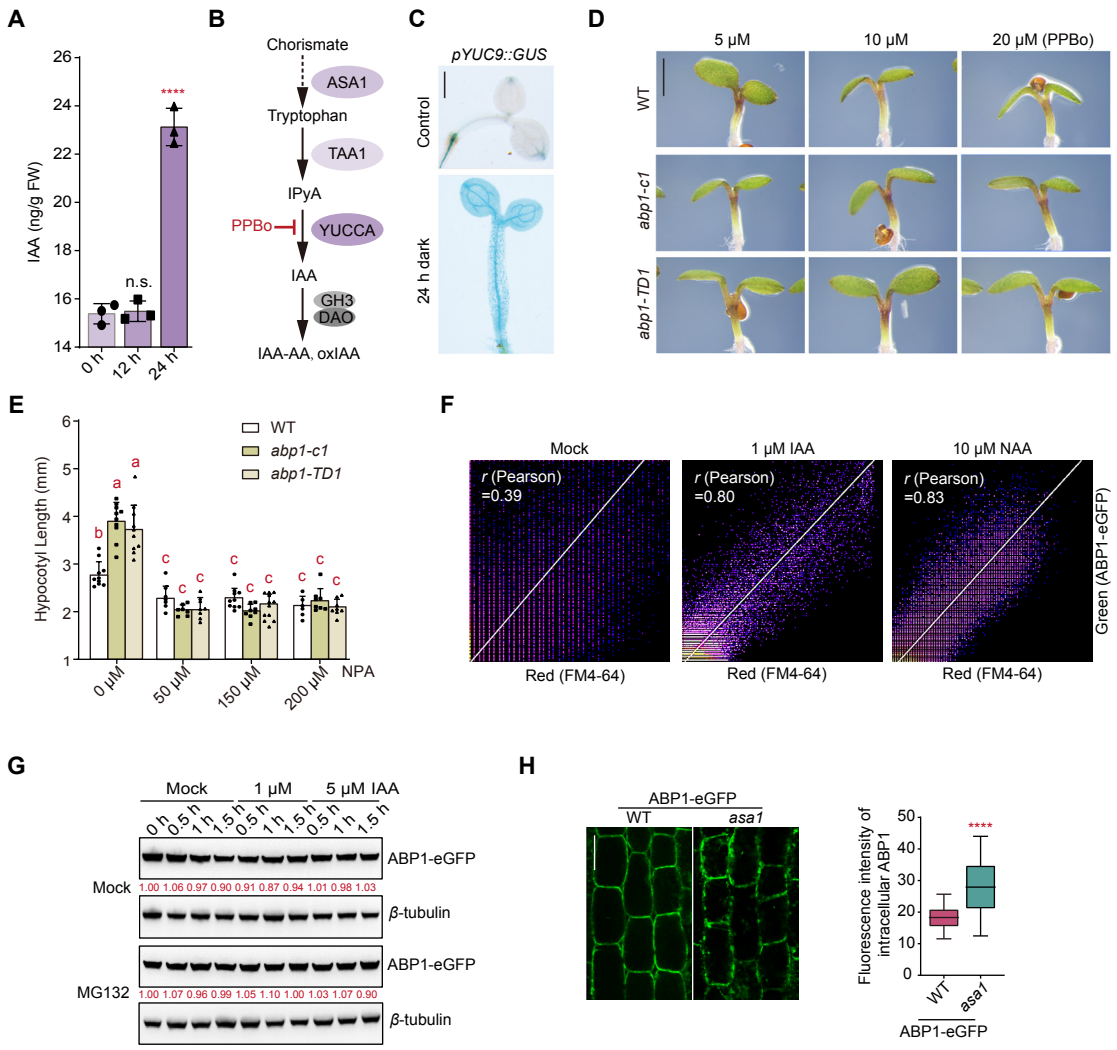

Figure S2. Dark treatment induces the trafficking of ABP1 through auxin, related to Figure 2

(A) Free IAA contents in aboveground tissue of 4-day-old seedlings subjected to darkness for 12 or 24 h. Data are presented as mean ± SD. Significant differences were determined using Student's *t*-test. ****$P < 0.0001$; n.s., not significant.

(B) Schematic representation of auxin biosynthesis pathway involving ASA1, TAA1 and YUCCA enzymes, with YUCCA activity inhibited by PPBo.

(C) GUS staining in 4-day-old *pYUC9::GUS* transgenic seedlings under normal light conditions (top) and after 24 h dark treatment (bottom). Scale bar, 1 mm.

(D) Phenotype of 4-day-old light-grown WT, *abp1-c1* and *abp1-TD1* seedlings followed by 36 h co-treatment of darkness and PPBo. Scale bar, 2 mm.

(E) Quantification of hypocotyl length in 4-day-old light-grown *abp1-c1* and *abp1-TD1* seedlings followed by 36 h co-treatment of dark and auxin inhibitor targeting *PIN*s, NPA. $n \geq 7$ hypocotyls.

(F) Scatterplot analysis of ABP1-eGFP and FM4-64 colocalization after IAA or NAA treatment. $n \geq 13$ cells from 3–4 hypocotyls. (*r*), Pearson's colocalization coefficient.

(G) Western blot showing the total protein levels of ABP1-eGFP in 4-day-old seedlings after IAA treatment at indicated period, with MG132 treatment as control. Numbers in red indicate protein amount of ABP1-eGFP after IAA treatment at each time point relative to non-treatment sample.

(H) Confocal microscopy imaging of ABP1-eGFP and fluorescence intensity of intracellular ABP1 in hypocotyl cortical cells of WT and *asa1* seedlings subjected to darkness for 18 h. Scale bar, 50 μm.

In (E, H), Data are presented as mean ± SD. Significant differences were determined using two-way ANOVA (E). Different lowercase letters indicate significant differences at $P < 0.05$. Significant differences were determined using Student's *t*-test (H). ****$P < 0.0001$.

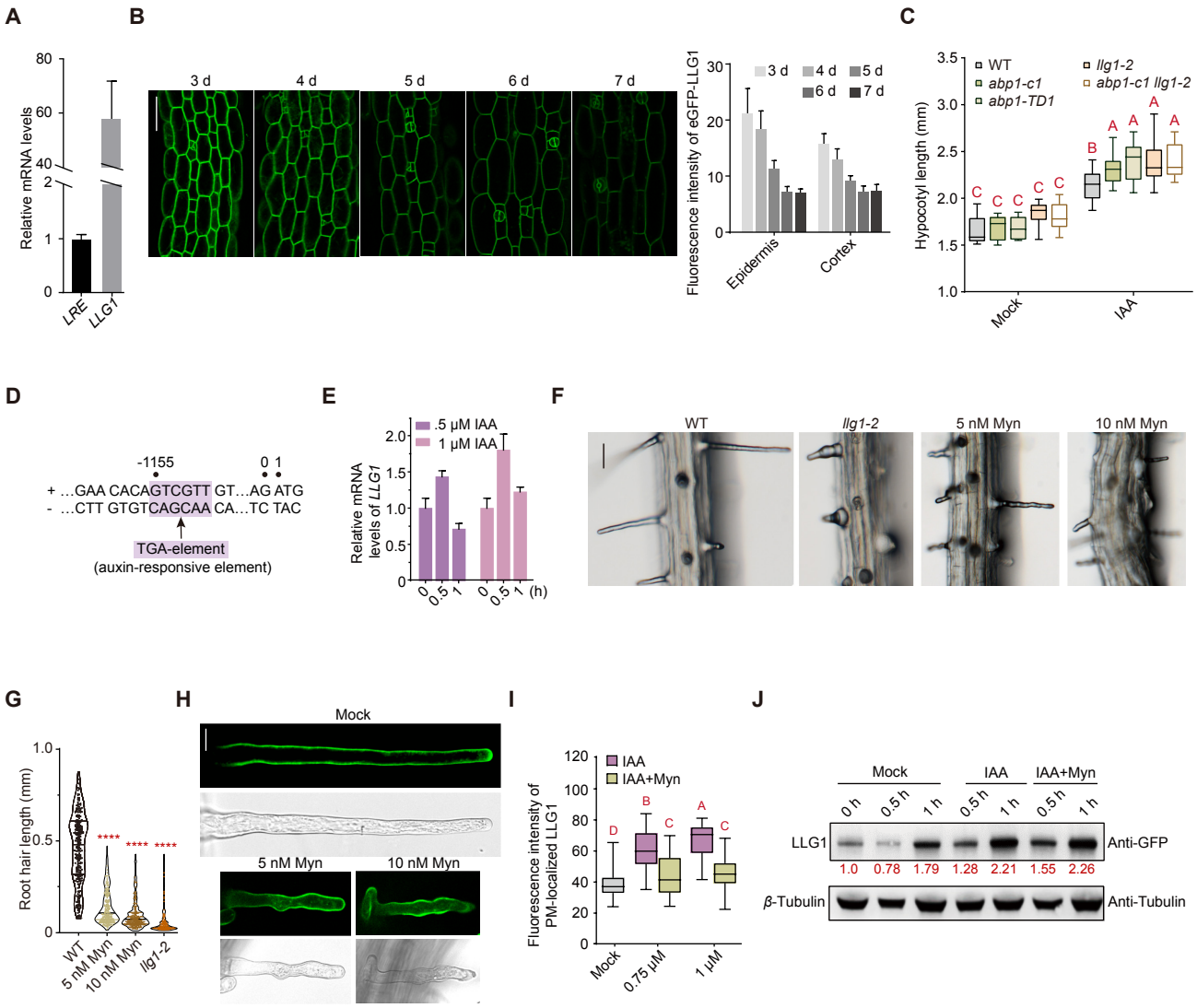

Figure S3. LLG1 promotes hypocotyl elongation via auxin signaling and Myn proteins restrain its trafficking, related to Figure 3

(A) RT-qPCR analysis of *LRE* and *LLG1* expression in the hypocotyl of 4-day-old seedlings.

(B) Confocal imaging showing the expression of LLG1 in hypocotyl cortical cells of *pLLG1:sp-eGFP-LLG1* transgenic plants from day 3 to 7. Scale bar, 50 μm. $n \geq 22$ seedlings. Time-course analysis of the fluorescence intensity of eGFP-LLG1 in hypocotyl epidermis and hypocotyl cortex from day 3 to 7.

(C) Quantification of hypocotyl length in WT, *abp1-c1*, *abp1-TD1*, *llg1-2* and *abp1-c1 llg1-2* seedlings under mock or IAA treatment for 12 h. $n \geq 9$ hypocotyls.

(D) Prediction in the *LLG1* promoter region showing an auxin-responsive element (TGA element).

(E) RT-qPCR analysis of *LLG1* expression in 4-day-old seedlings after IAA treatment for 0.5 or 1 h.

(F–G) Phenotype and quantification of root hair length in 3.5-day-old WT (with/without Myn treatment) and *llg1-2* (untreated) seedlings. Scale bar, 50 μm. $n \geq 149$ root hairs from 10 roots.

(H) LLG1 localization in root hair of 3.5-day-old *pLLG1:sp-eGFP-LLG1* transgenic seedlings with/without Myn treatment. Scale bar, 20 μm.

(I) Quantification of fluorescence intensity of PM-localized eGFP-LLG1 in hypocotyl epidermal cells of 4-day-old *pLLG1::sp-eGFP-LLG1* transgenic seedlings treated with IAA alone or together with Myn. $n \geq 12$ cells from 3–4 hypocotyls.

(J) Western blot showing the total protein levels of eGFP-LLG1 in 4-day-old seedlings treated with 1 μM IAA alone or Myn co-treatment. Numbers in red indicate protein amount of eGFP-LLG1 after treatment at each time point relative to non-treatment sample.

In (C, G, I), data are presented as mean ± SD. Significant differences were determined using two-way ANOVA (C, I). Different uppercase letters indicate significant differences at $P < 0.01$. Significant differences were determined using Student's *t*-test (G). ****$P < 0.0001$

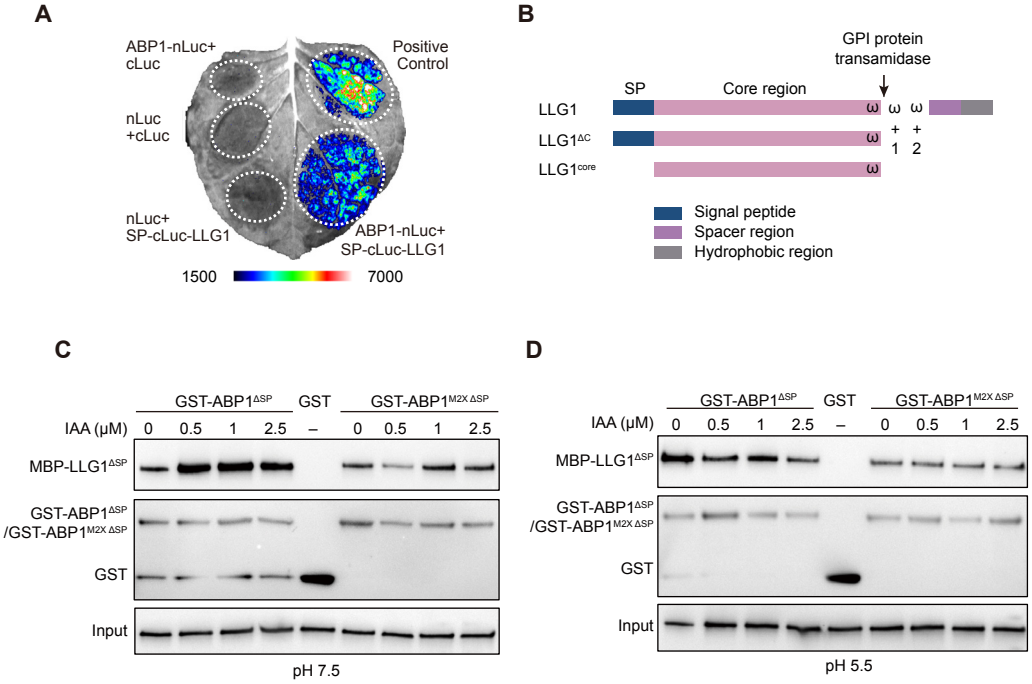

Figure S4. ABP1 and LLG1 exhibit direct physical interaction, related to Figure 4

(A) Luciferase complementation assay showing the interaction between full-length ABP1 and full-length LLG1. SP, signal peptide.

(B) The *LLG1* gene model, illustrating the predicted protein features, including the N-terminal signal peptide and the C-terminal GPI-anchor processing sites (ω-sites).

(C–D) Pull-down assay showing ABP1$^{\Delta SP}$–LLG1$^{\Delta SP}$ or ABP1$^{M2X\ \Delta SP}$–LLG1$^{\Delta SP}$ interaction after IAA treatment under pH 7.5 or pH 5.5.

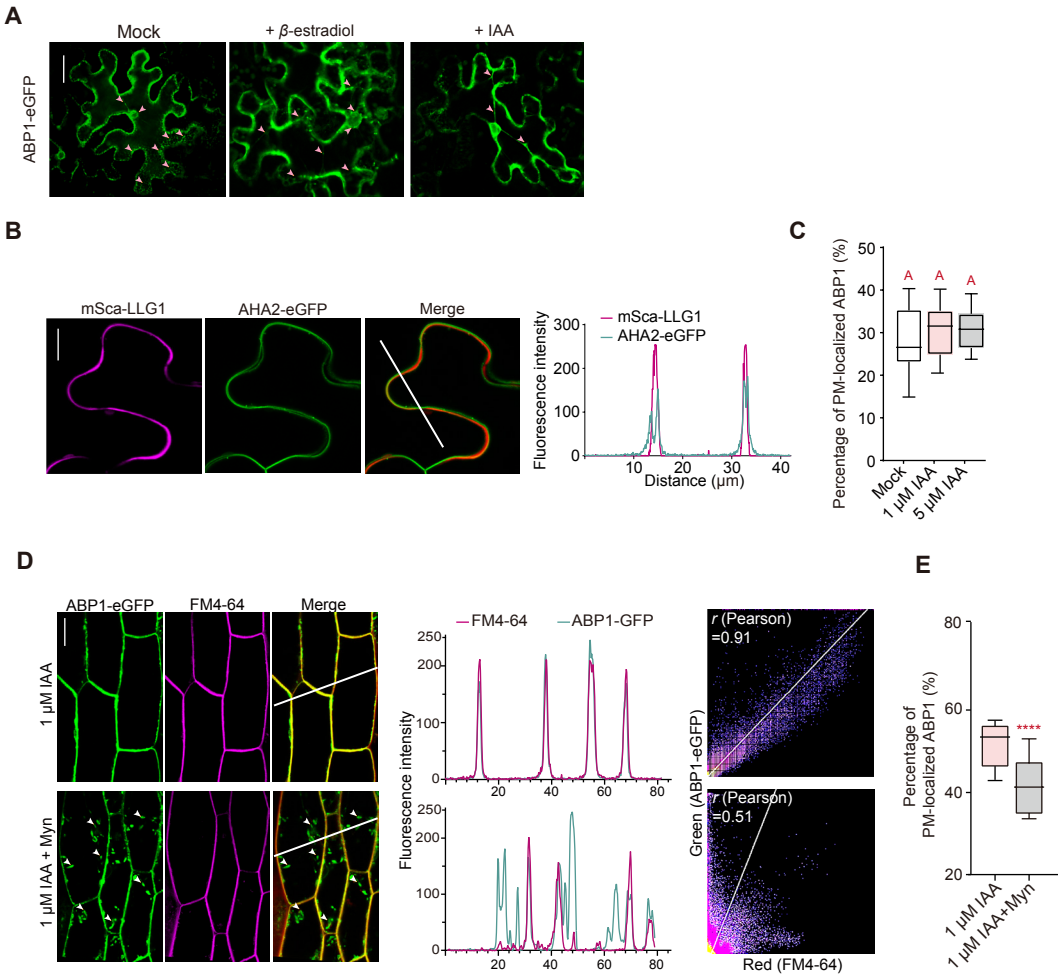

Figure S5. LLG1 chaperones ABP1 transportation through GPI-AP pathway, related to Figure 5

(A) Fluorescence imaging showing the expression of ABP1-eGFP alone under mock condition and treated with *β*-estradiol for 24 h or 1 μM IAA for 35 min in *N. benthamiana* leaves. Pink arrowheads indicate the ER regions. Scale bar, 20 μm.

(B) Confocal microscopy imaging and fluorescence plot profiles of mSca-LLG1 and PM marker AHA2-eGFP. White line indicates the region for fluorescence intensity measurement. Scale bar, 10 μm.

(C) The percentage of ABP1-eGFP localized to PM showing the colocalization of FM4-64 and ABP1-eGFP in *llg1-1* background after IAA treatment for 1 h. $n \geq 42$ cells from 15 hypocotyls.

(D) Confocal microscopy imaging (left), fluorescence plot profiles (middle) and scatterplot analysis with Pearson's colocalization coefficient (right) of ABP1-eGFP in hypocotyl epidermal cells of 4-day-old seedlings treated with IAA alone or Myn co-treatment for 1 h. White lines are used for fluorescence intensity measurement. White arrowheads indicate the punctate signals in ER. Scale bar, 20 μm.

(E) The percentage of ABP1-eGFP localized to PM relative to total protein in 4-day-old seedlings treated with IAA alone or Myn co-treatment. $n = 5$ hypocotyls.

In (C, E), data are presented as mean ± SD. Significant differences were determined using one-way ANOVA (C) or Student's *t*-test (E). Different uppercase letters indicate significant differences at $P < 0.01$. ****$P < 0.0001$.

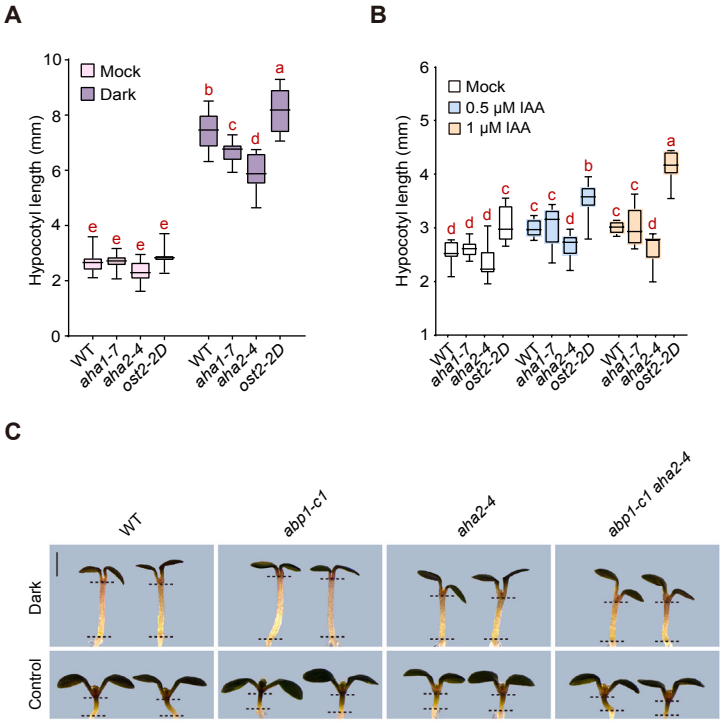

Figure S6. **AHA1/2 regulate hypocotyl elongation under dark and auxin treatment, related to Figure 6**

(A) Quantification of hypocotyl length in *aha1-7*, *aha2-4* and *ost2-2D* seedlings subjected to darkness treatment for 30 h. $n \geq 16$ seedlings.

(B) Quantification of hypocotyl length in *aha1-7*, *aha2-4* and *ost2-2D* seedlings treated with/without IAA for 30 h. $n \geq 7$ seedlings.

(C) Phenotype of hypocotyl length in WT, *abp1-c1*, *aha2-4* and *abp1-c1 aha2-4* seedlings subjected to darkness for 30 h. $n \geq 23$ seedlings. Scale bar, 2 mm.

In (A–B), data are presented as mean ± SD. Significant differences were determined using two-way ANOVA. Different lowercase letters indicate significant differences at $P < 0.05$.

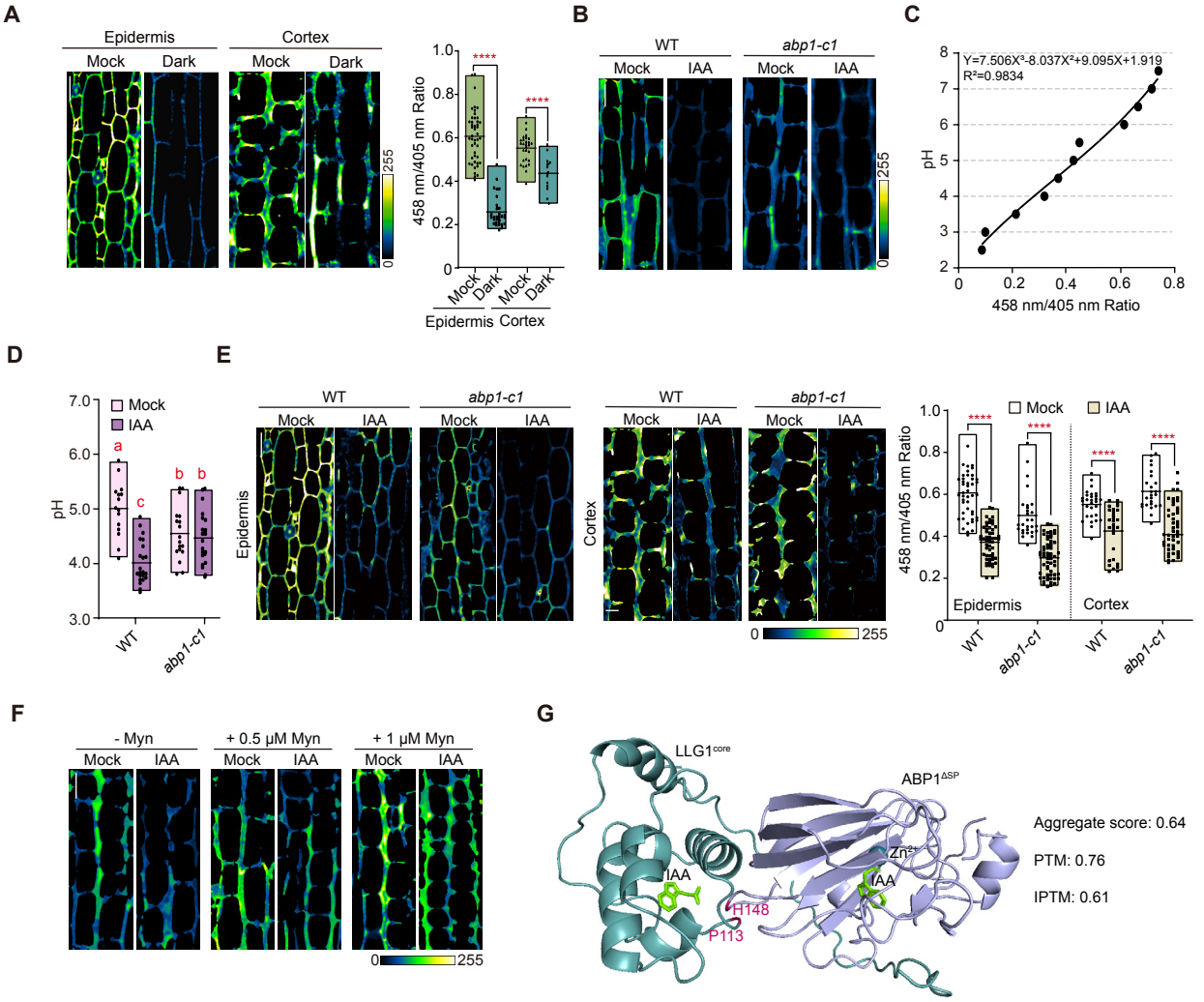

Figure S7. ABP1 regulates dark-induced apoplast acidification in hypocotyl, related to Figure 6

(A) Confocal imaging and relative quantification of HPTS-stained apoplastic pH in hypocotyl epidermal and cortical cells in 4-day-old WT seedings subjected to darkness for 18 h. $n \geq 15$ cells. Scale bar, 40 μm.

(B) Confocal imaging of HPTS-stained apoplastic pH in hypocotyl cortex cells in 4-day-old WT and *abp1-c1* seedlings after dark treatment for 18 h following 1 μM IAA treatment for 15 min. Scale bar, 40 μm.

(C) *In vivo* calibration curve of apoplastic pH.

(D) Relative quantification of apoplastic pH in hypocotyl cortical cells of 4-day-old WT and *abp1-c1* seedlings subjected to darkness for 18 h, followed by 1 μM IAA treatment for 15 min. HPTS-stained pH values were calculated using a standard curve.

(E) Confocal imaging and relative quantification of HPTS-stained pH in the apoplast of hypocotyl epidermal and cortical cells in 4-day-old light-grown WT and *abp1-c1* seedlings treated with 1 μM IAA for 15 min. $n \geq 25$ cells. Scale bar, 40 μm.

(F) Confocal imaging of HPTS-stained pH in the apoplast of hypocotyl cortical cells in 3-day-old WT seedlings treated with Myn for 1 d followed by 18 h dark treatment and then 1 μM IAA treatment for 15 min. Scale bar, 40 μm.

(G) Structural model of the LLG1–ABP1 interaction in the presence of IAA predicted by Chai-1 docking. $LLG1^{core}$ protein is colored deep teal and $ABP1^{\Delta SP}$ is colored light blue. The auxin molecule IAA is shown in green. The predicted key residues P113 in LLG1 and H148 in ABP1 are highlighted in hot pink.

In (A, D–E), data are presented as mean ± SD. Significant differences were determined using Student's *t*-test (A, E) or two-way ANOVA (D). ****$P < 0.0001$. Different lowercase letters indicate significant differences at $P < 0.05$.

STAR ⭐ METHODS

Detailed methods are provided in the online version of this paper and include the following:

- KEY RESOURCES TABLE
- RESOURCE AVAILABILITY
  - Lead contact
  - Materials availability
  - Data and code availability
- EXPERIMENTAL MODEL AND SUBJECT DETAILS
  - Plant Material and Growth Conditions
- METHOD DETAILS
  - Dark treatment and hypocotyl growth examination
  - Auxin treatment and hypocotyl length measurement
  - Measurement of free IAA levels
  - Histochemical GUS staining assay
  - Plasmid construction and generation of transgenic plants
  - Plant protein extraction and western blot
  - RNA isolation, RT-PCR, and qRT-PCR analysis
  - Confocal microscopy imaging
  - Colocalization analysis
  - Luciferase complementation assay
  - Protein expression and purification
  - Pull-down assays
  - FRET-FLIM assay
  - HPTS staining and imaging
  - *In vivo* phosphorylation assay
  - Protein structure prediction and small-molecule docking
- QUANTIFICATION AND STATISTICAL ANALYSIS

SUPPLEMENTAL INFORMATION

ACKNOWLEDGMENTS

The project was supported by grants from National Natural Science Foundation of China (32425008, 32230009) and Science and Technology Commission of Shanghai Municipality (24N12800100). We express our sincere gratitude to Dr. Peng Zhang and Dr. Xue Zhang for assistance with structural prediction analysis; Dr. Lin Li and the Large-Scale Instrument Sharing Platform of the School of Life Sciences at Fudan University for support with hypocotyl growth kinetic analysis. We thank Dr. Jiří Friml for providing the seeds of *pABP1:GFP-ABP1-M2X*/*abp1-c1*, Dr. Lin Xu for *abp1-c1* and *abp1-TD1,* Dr. Jun Liu for *ost2-2D,* Dr. Meng-xiang Sun for RFP-HDEL and Dr. Peng Zhao for mScarlet-K32 vector. We also acknowledge the Institute of Genetics and Developmental Biology, CAS for IAA quantification assay and the Materials Characterization Center and the Instruments Sharing Platform of School of Life Sciences, East China Normal University.

AUTHOR CONTRIBUTIONS

C. L. conceived and supervised the project. J.W. conducted all experiments. J-P.Y. conducted genotyping, AHA-related analysis. C.L., J.W. and J-P.Y. prepared the manuscript. M-M.Z. and Y-Z.H. conducted GPI-AP trafficking analysis. H-Q.F. and M-Z.L. conducted initial ABP1-LLG1 functional analysis. T-D.X. contributed to the mechanistic interpretation and edited manuscript. B-Y.L. contributed to the preliminary investigation for this project.

DECLARATION OF INTERESTS

The authors declare no conflict of interest.

STAR ⭐ METHODS

KEY RESOURCES TABLE

RESOURCE AVAILABILITY

Lead contact

Requests for further information and resources should be directed to and will be fulfilled by the lead contact, Chao Li (cli@bio.ecnu.edu.cn).

Materials availability

The *Arabidopsis* genetic transformation materials constructed in this study are available upon request.

Data and code availability

Data supporting the findings of this study are available within the paper. Source data (all gels and graphs) are provided with this paper. This study did not generate any code information.

EXPERIMENTAL MODEL AND STUDY PARTICIPANT DETAILS

Plant materials and growth conditions

Arabidopsis ecotype Col-0 was used as wild type in this study. The *abp1-c1*, *abp1-TD1(Gao et al., 2015)*, *llg1-2*(Li et al., 2015), *aha1-7*, *aha2-4(Liu et al., 2025a)*, *ost2-2D(Sylvain Merlot, 2007)*and *pYUC9:GUS(Chen et al., 2016)* have been described previously. Seeds were surface-sterilized with 75% (v/v) ethanol for 5 min, followed by five times washes with sterilized distilled water. The sterilized seeds were then germinated on plates containing half-strength Murashige and Skoog (1/2 MS) medium supplemented with 1% (w/v) sucrose and solidified with 0.8% (w/v) agar, adjusted to pH 5.7. *Arabidopsis* seedlings were cultivated in Percival growth chambers under controlled environmental conditions (hereafter, standard growth conditions): 16-h light/8-h dark photoperiod with 22°C light/20°C dark temperatures and 60% relative humidity. The light regimes were implemented under regular white light at an intensity of 100 μmol m^{-2} s^{-1}.

METHOD DETAILS

Dark treatment and hypocotyl growth examination

The kinetics of hypocotyl growth were monitored using the high-throughput imaging platform DynaPlant® at the School of Life Sciences, Fudan University. Seeds were sown on 1/2 MS medium solidified with 2% phytagel (Solarbio, P8170). 3-day-old seedlings were pretreated under continuous white light for 24 h for acclimation to fresh medium, and subsequently transferred to complete darkness for 36 h. During dark incubation, hypocotyl growth was imaged at 15 min intervals using the DynaPlant® system with a spatial resolution of 1.2 μm per pixel. Hypocotyl growth lengths in the time-series images were quantified by DynaPlant Analysis software (provided by the instrument manufacturer). Data are presented as mean ± SEM. Means were calculated from hypocotyls of more than 28 seedlings. Experiments were performed with at least three biological replicates, with each replicate derived from distinct biological samples to minimize batch effects.

Hypocotyl imaging was conducted using a stereomicroscope (Leica M205 FCA) and a fluorescence microscope (Leica DM2500) equipped with a 20× water-immersion objective. Hypocotyl length was measured in ImageJ from the axillary bud to the hypocotyl-root junction. For cellular analyses, individual cell areas were quantified by tracing cell boundaries using the polygon selection tool in ImageJ.

4-Phenoxyphenylboronic acid (Kakei et al., 2015) (PPBo, MedChemExpress, HY-76584) or N-1-Naphthylphthalamic acid (Yang et al., 2022) (NPA, MedChemExpress, HY-116425) was added to solid 1/2 MS medium at specified concentrations for dark treatment. 4-day-old seedlings grown under standard conditions were transferred to the respective plates, which were then wrapped in two layers of aluminum foil to ensure complete darkness and placed vertically in Percival growth chambers. Hypocotyl imaging and length measurement were performed as described above.

Auxin treatment and hypocotyl length measurement

Seedlings were treated with liquid 1/2 MS medium (1% sucrose, pH 5.7), supplemented with indicated concentrations of indole-3-acetic acid (IAA, Sigma-Aldrich, I2886). All treatments were performed in 1.5 mL Eppendorf tubes under standard growth conditions with continuous white light (~100 $\mu mol \cdot m^{-2} \cdot s^{-1}$). For IAA treatment of cotyledons, lanolin (Aladdin, L116309) was used as the medium, as outlined in established protocols (Bellstaedt et al., 2019). Briefly, lanolin was melted at 65°C, mixed with 1mM IAA (at the desired concentrations) or DMSO, and homogenized thoroughly. Seedlings were then vertically positioned (adaxial-side down) in the lanolin-IAA mixture to ensure uniform cotyledon coating before solidification. The treated seedlings were then transferred to 1/2 MS solid medium and cultured vertically under standard growth conditions. The means were calculated from at least 9 hypocotyls. Experiments were performed with at least three biological replicates, with each replicate derived from distinct biological samples to minimize batch effects.

Measurement of free IAA levels

Seedlings were grown for 4 days under standard conditions and then transferred to darkness for 0, 12 or 24 h. For the quantification of phytohormone IAA, approximately 200 mg mixture of cotyledon and hypocotyl tissues were harvested and spiked with 3 ng [$^{13}C_6$] IAA internal standard. Samples were subjected to extraction, purification, and methylation prior to analysis by selected-ion-monitoring GC-MS following established protocols (Barkawi et al., 2008). The measurement was performed as previously described (Sun et al., 2016) in the Institute of Genetics and Developmental Biology, Chinese Academy of Sciences.

Histochemical GUS staining assay

For GUS staining assay, seedlings were incubated in buffer containing 100 mM sodium phosphate buffer (pH 7.0), 10 mM EDTA, 0.1% (v/v) Triton X-100, 0.5 mM potassium ferricyanide, 0.5 mM potassium ferrocyanide and 1 mM X-Gluc at 37°C in darkness for 12 h, followed by incubation in 70% ethanol for 5 h with the ethanol replaced every hour. The samples were photographed under a stereoscope (Leica M205 FCA).

Plasmid construction and generation of transgenic plants

Primers used in this study can be found in Table S1. Full-length ABP1 and LLG1 cDNAs were PCR-amplified from Col-0 for subsequent cloning. For plant transformation, the genes were cloned into

675 *pCAMBIA1300* to generate *pLLG1:sp-eGFP-LLG1* and *pABP1:ABP1-eGFP* constructs, which
676 were subsequently introduced into *llg1-2* mutant and Col-0 plants respectively using *Agrobacterium*
677 *tumefaciens* (strain GV3101)-mediated floral dip transformation(Clough and Bent, 2008). For
678 protein interaction studies, the cDNAs were first cloned into *pDONR221* vectors (*P3P2-ABP1* and
679 *P1P4-LLG1*) using BP recombination, then recombined into the pFRETtv-2in1-CC7 vector
680 (Addgene 105116) to create the FRET reporter construct *pFRET-ABP1-mTurquoise2–LLG1-*
681 *mVenus*. Additionally, ABP1 was subcloned into *pGEX-6P-1* for prokaryotic expression in
682 *Escherichia coli* (Rosetta, BL21).

683 For *SP-cLuc-LLG1*, sequences encoding the signal peptide of LLG1 (residue 1–23), nLuc, and
684 the deleted signal peptide of LLG1 (residues 24–168) were amplified by PCR and cloned into
685 *pCAMBIA1300* driven by the 35S promoter using a ClonExpress II One Step Cloning Kit. For *SP-*
686 *cLuc-LLG1*$^{\Delta GPI}$, sequences encoding the signal peptide of LLG1 (residue 1–23), nLuc, and the
687 deleted cytoplasmic domain of LLG1 (residues 24–147) were amplified. For *ABP1-nLuc*, sequences
688 encoding the ABP1 (residues 1–198) was fused with cLuc. For *ABP1*$^{\Delta KDEL}$, sequences encoding the
689 ABP1 (residues 1–194) was fused with cLuc. Primers used in plasmid construction are listed in
690 Table 1 (Supporting Information).

691 For *sp-mScarlet-LLG1 (XVE),* sequences encoding the signal peptide of LLG1 (residue 1–23),
692 mScarlet, and the deleted signal peptide of LLG1 (residues 24–168) were amplified by PCR and
693 cloned into *pER8* vector of the *XVE* inducible system (Jianru Zuo, 2000) using a ClonExpress II
694 One Step Cloning Kit. In transgenic tobacco leaves, estradiol-activated *XVE* induces expression of
695 the *mScarlet* reporter gene driven by a target promoter consisting of eight copies of the LexA
696 operator fused upstream of the −46 35S minimal promoter.

697 For *pAHA2:AHA2/aha2-4*, full-length AHA2 cDNA was PCR-amplified from Col-0 seedlings
698 for subsequent cloning. To generate the native promoter-driven complementation construct, the
699 AHA2 genomic fragment containing the promoter region and coding sequence was cloned into the
700 binary vector pCAMBIA1300 to produce *pAHA2:AHA2*. For the phospho-deficient mutant
701 construct *pAHA2:AHA2*$^{T881A/T947A}$*/aha2-4*, site-directed mutagenesis was performed to substitute
702 Thr881 and Thr947 with alanine residues (T881A and T947A). The mutated AHA2 fragment was
703 then cloned into pCAMBIA1300 under the control of the native AHA2 promoter to
704 generate *pAHA2:AHA2*$^{T881A/T947A}$. The resulting constructs were introduced into the *aha2-4* mutant
705 background via Agrobacterium tumefaciens (strain GV3101)-mediated floral dip transformation,
706 and transgenic lines were selected on hygromycin-containing medium for further analysis.

707 **Plant protein extraction and western blot**

708 For the detection of changes in protein levels, plant tissue samples from specific periods and
709 treatments were harvested and ground in liquid nitrogen. Total proteins were extracted using Tris-
710 HCl buffer (pH 6.8) through sequential centrifugation (15,000 × g, 30 min; then 15,000 × g, 10 min)
711 at 4°C. For MG132 (MedChemExpress, HY-13259) treatment, it was diluted with 1/2 MS liquid
712 medium to 30 μM and applied 30 min prior to IAA treatment. Protein samples were quantified by
713 BCA assay, mixed with loading buffer, and heat-denatured at 99°C for 10 min.

714 Plasma membrane (PM) proteins were extracted using a commercial kit (Solarbio, China,
715 EX2080). Protease inhibitor cocktail (2 μL) was added to 500 μL of cold Extraction Buffer A, mixed

716 thoroughly, and kept on ice. Plant tissue (100–200 mg) was finely chopped and homogenized in 500
717 μL of Extraction Buffer A at 2–8°C. The homogenate was transferred to a pre-cooled centrifuge tube,
718 shaken at 2–8°C for 30–60 min, and then centrifuged at 12,000 × g for 5 min at 2–8°C. The
719 supernatant was collected, mixed with 5 μL of Extraction Buffer B, incubated at 37°C for 10 min,
720 and centrifuged at 1,000 × g for 3 min at 37°C. After removing the upper layer, the remaining 30–
721 50 μL lower phase was dissolved in 50–150 μL ice-cold Membrane Protein Solubilization Buffer C
722 to obtain the membrane protein fraction.

723 Endoplasmic reticulum (ER) proteins were extracted using a commercial kit (Solarbio, China,
724 EX2061). Briefly, protease inhibitor cocktail was added to Extraction Buffer C (2 μL per 300 μL),
725 mixed, and kept on ice. Approximately 200–500 mg of plant tissue (de-veined and cleaned) was
726 finely chopped, homogenized in 1 mL Extraction Buffer A using a homogenizer or Dounce
727 homogenizer, and filtered through a 100 μm cell strainer. The filtrate was sequentially centrifuged
728 at 200 × g for 3 min, 500 × g for 5 min, 1000 × g for 10 min, and 20,000 × g for 10 min, collecting
729 the supernatant at each step. This was followed by ultracentrifugation at 50,000 × g for 45 min to
730 pellet microsomal membranes (using a benchtop ultracentrifuge, Thermo Sorvall MTX150). The
731 pellet was resuspended in 400 μL of cold Reagent B, centrifuged again at 50,000 × g for 45 min,
732 and the resulting pellet was resuspended in 200–300 μL of Extraction Buffer C. After shaking at 2–
733 8 °C for 30 min, the mixture was centrifuged at 12,000 × g for 10 min at 4 °C. The supernatant
734 containing ER proteins was collected, quantified, aliquoted, and stored at −80 °C for further use.

735 For Western blot detection, anti-GFP (1:2000 dilution, sc-9996, Santa Cruz, America) was used
736 to detect eGFP-LLG1 or ABP1-eGFP fusion protein expression. Anti-Bip (1:2000 dilution, Agrisera,
737 AS09481, Sweden) was used as an ER reference protein. Anti-AHA2 (1:1000 dilution, PY231,
738 Beijing QiWei YiCheng Tech Co., Ltd) was used as a PM reference protein. HRP-conjugated Goat
739 Anti-Mouse IgG (1:5000 dilution, Sangon Biotech, D110087) or HRP-conjugated Goat Anti-Rabbit
740 IgG (1:5000 dilution, Sangon Biotech, D110058) was used as the secondary antibody.

741 **RNA isolation, RT-PCR, and qRT-PCR analysis**

742 Seedlings at appropriate developmental stages were harvested, and roots were excised to retain only
743 aboveground parts for transcript profiling of *ABP1* and *LLG1/LRE* genes. RNA was extracted using
744 the RNAprep Pure Plant Kit (TIANGEN, China), and first-strand cDNA was synthesized with a
745 HiScript ®II 1st Strand cDNA Synthesis kit (Vazyme, China). qRT-PCR was performed with
746 ChamQ Universal SYBR qPCR Master Mix (Vazyme, China) using the following thermal profile:
747 95°C for 5 min, 30 cycles of 95°C for 10 s and 60°C for 30 s. Relative transcript levels were
748 calculated using the $2^{-\Delta\Delta CT}$ method, normalized to *ACTIN2*. Primer sequences are listed in Table 1
749 (Supporting Information).

750 **Confocal microscopy imaging**

751 For colocalization analysis in *Arabidopsis thaliana* and *N. benthamiana*, images were acquired by
752 the Ultra High Resolution Laser Leica STELLARIS 8 confocal microscope with WLL laser, power
753 HyD detector (HyDx, HyD2 and HyD3) and frame scanning mode. The real fluorescence signal was
754 determined using TauGating (time-gated fluorescence lifetime filtering) and counting techniques as
755 capture modes. TauGating was applied to suppress autofluorescence, and photon counting mode
756 was used to enhance signal-to-noise ratio (Kriechbaumer et al., 2018). No fluorescence signal was

detected in Col-0 seedlings under identical imaging settings and channels. Intracellular ER was visualized using RFP-HDEL (Gomord V, 1997) as an ER marker, while PM was stained with the lipophilic dye FM4-64 (Liu et al., 2024), allowing simultaneous visualization of both compartments. For various fluorescent proteins, GFP, Ex 490 nm, Em 505–560 nm; RFP, Ex 532nm, Em 550–700 nm; FM4-64, Ex 523nm, Em 550–700 nm; mScarlet, Ex 594, Em 628 nm. All imaging sessions, including mock controls and experimental samples (IAA or NAA treatment; NAA, Sigma-Aldrich, N0640), were acquired using identical instrument settings: laser power (20% WLL output) and environmental conditions (21℃ with 35% humidity). The statistics were calculated from more than 3 cells in approximately 3–4 independent hypocotyls. Each cell area included the complete cell edge, and the same calculation parameters and procedures were used for all cells. Experiments were performed with at least three biological replicates, with each replicate derived from distinct biological samples to minimize batch effects.

Myriocin (Myn, GLPBIO, GC14278, Montclair, CA, USA) was added to the solid medium for cultivating *Arabidopsis thaliana* seedlings. 10 μM *β*-estradiol (Sigma-Aldrich E2758) was pressure-infiltrated into Agrobacterium-transformed tobacco leaves 24 h post-transformation, with phenotypic analysis performed 24 h post-induction.

Colocalization analysis

Colocalization was quantified in Fiji software using the Coloc 2 plugin (Analyze › Colocalization Analysis › Coloc 2), yielding colocalization scatter plots, Pearson coefficients. For each sample, paired green and red channel images were loaded, and regions of interest (ROIs) were selected for analysis. Pearson's correlation coefficients (r), ranging from −1 (perfect negative correlation) to +1 (perfect positive correlation)(Adler and Parmryd, 2010), were calculated to quantify the degree of signal colocalization. Pearson's correlation coefficients (r) were computed as follows:

$$r = \frac{\sum (R_i - R_{av}) \cdot (G_i - G_{av})}{\sqrt{\sum (R_i - R_{av})^2 \cdot \sum (G_i - G_{av})^2}}$$

R_i, G_i represent the intensity values of the i-th pixel in the red channel (R_i) and green channel (G_i). R_{av}, G_{av} represent the mean intensities of the entire dataset for the red channel (R_{av}) and green channel (G_{av}).

To obtain the colocalization peak plots, merged dual-fluorescence images were converted to color channels: Image > color > channel tool > color channel. A straight line was used to mark the region of interest, and the plot profile's live mode was employed to display the fluorescence peak plots of different channels. The data were saved separately and graphed in GraphPad Prism.

Luciferase complementation assay

Agrobacterium tumefaciens strain GV3101 harboring various constructs was cultured in LB liquid medium until reaching an OD_{600} of 1.0. The cultures were then centrifuged at 3,824 × g for 10 min, and the resulting pellets were washed and resuspended in double-distilled water supplemented with 10 mM MES (pH 5.7), 10 mM $MgCl_2$, 0.01% Tween-20 and 100 μM acetosyringone to a final OD_{600} of 0.6. Equal volumes of bacterial suspensions containing the nLUC and cLUC constructs were mixed and infiltrated into designated regions of *Nicotiana benthamiana* leaves. Plants were kept in darkness for 12 h, then transferred to a 16-h light/8-h dark cycle for an additional 48 h. To assess

796 luciferase activity, infiltrated leaves were treated with a luciferin solution [1 mM luciferin, 0.05%
797 (v/v) Triton X-100] and incubated in the dark for 5 min, followed by imaging using a Tanon-5200
798 Multi chemiluminescence/fluorescence imaging system (Tanon, China) equipped with a cooled
799 CCD camera.

800 **Protein expression and purification**

801 DNA sequences encoding LLG1 (residues 24–168) and ABP1 (residues 34–198) were cloned into
802 the pMAL-c5x or pGEX-6P-1 vectors for expression in *E. coli* BL21 Competent Cells. For MBP-
803 and GST-tagged proteins, cells were incubated at 37°C with shaking at 200 rpm until the OD_{600}
804 reached 0.6. Following induction with 0.5 mM isopropyl-β-d-thiogalactopyranoside (IPTG), cells
805 were incubated with shaking for 3 h at 37°C (MBP-LLG1) or 16 h at 25°C (GST-ABP1), and
806 harvested by centrifugation at 3,824 × g for 10 min at 4°C. Cells were lysed by sonication on ice in
807 lysis buffer containing 50 mM Tris-HCl pH 7.5, 100 mM NaCl, 1 mM Na_2-EDTA, 5% (v/v) glycerol ,
808 and 1 mM PMSF, and centrifuged at 15,000 rpm for 30 min at 4°C. The supernatants were purified
809 using amylose resin (YESEN, China) for MBP fusion protein and glutathione agarose resin (YESEN,
810 China) for GST fusion protein.

811 **Pull-down assays**

812 For the GST pull-down assay, purified MBP-LLG1$^{\Delta SP}$ and GST-ABP1$^{\Delta SP}$ (GST-ABP1$^{\Delta SP\ S106A}$, GST-
813 ABP1$^{\Delta SP\ T146A}$, GST-ABP1$^{\Delta SP\ H148A}$) proteins were resuspended in binding buffer (50 mM Tris-HCl
814 pH 5.5/6.0/6.5/7.0/7.5/8.5, 100 mM NaCl, 1 mM Na2-EDTA, 5% (v/v) glycerol, 1 mM PMSF) and
815 incubated with GSTSep Glutathione Agarose Resin (Yeasen, 20507ES10) at 4°C for 2 h with
816 rotation. The resins were then washed three times in pull-down buffer, followed by the addition of
817 SDS-PAGE loading buffer and boiled for 5 min, and used for immunoblot analysis. The protein blot
818 was stained with Ponceau S for loading detection. Anti-MBP antibody (D195305-0100, 1:2,000
819 dilution, Sangon Biotech, China), anti-GST horseradish peroxidase-conjugated antibody (B-14,
820 1:1,000 dilution, Santa Cruz Biotechnology, USA), and anti-mouse secondary antibody (ASS1007,
821 1:5,000 dilution, Abgent, USA) were used for chemiluminescence detection. The signals were
822 acquired using the Tanon-2500R imaging system (China).

823 **FRET-FLIM assay**

824 Tobacco (*Nicotiana benthamiana*) leaves were agroinfiltrated to co-express ABP1-mTurquoise2
825 (donor) and LLG1-mVenus (acceptor) constructs. Imaging was performed 48–72 h post-infiltration
826 on epidermal cells exhibiting dual fluorescence signals. Confocal laser scanning microscopy (CLSM)
827 settings were as follows: excitation 458 nm/emission 465 to 505 nm (mTurquoise2), excitation 514
828 nm/emission 520 to 560 nm (mVenus). Cells of interest were selected using a 40× water-immersion
829 objective. ABP1-mTurquoise2 was used as the donor only. The fluorescence lifetime of the donor
830 (mTurquoise2) was measured using the FLIM (Bücherl et al., 2014) module (PicoHarp 300 TCSPC
831 system), with the average value obtained from three measurements as the initial fluorescence
832 lifetime of the donor. The efficiency of mTurquoise2–mVenus FRET was analyzed using a STED
833 Leica microscope with the FRET module. The region of interest (ROI) was selected to focus on the
834 specific subcellular regions, and the initial fluorescence lifetime value of the donor was inputted.
835 FRET efficiency was automatically calculated by the system using the following formula:

836 $$E_{(FRET-FLIM)} = 1 - \frac{\tau(quench)}{\tau} = 1 - \frac{\tau(donor, FRET)}{\tau(donor, no\ FRET)}$$

837 τ (donor, FRET) represents the donor lifetime in the presence of the acceptor, and τ (donor, no FRET)
838 represents the donor lifetime in the absence of the acceptor(Bücherl et al., 2014).

839 **HPTS staining and imaging**

840 HPTS staining(Amali et al., 2011; Liu et al., 2025b) and imaging were performed as described by
841 Lin(Lin et al., 2021) with modifications. Prior to staining, hypocotyls of 4-day-old light-grown
842 seedlings or seedlings subjected to 18 h of darkness were equilibrated in 1/2 MS growth medium
843 supplemented with 0.2 mM MES for at least 30 min. For auxin treatment, hypocotyls were incubated
844 in 1/2 MS growth medium supplemented with 5 mM HPTS (prepared from a 100 mM aqueous stock
845 solution) and 1 μM IAA for 15 min. For Myn treatment, seedlings were grown on 1/2 MS medium
846 under continuous light for 3 days and then transferred to 1/2 MS solid medium supplemented with
847 different concentrations of Myn for pre-incubation for 24 h. Subsequently, seedlings were subjected
848 to co-treatment with Myn under dark conditions for 18 h, after which hypocotyls were incubated in
849 1/2 MS growth medium containing 5 mM HPTS and 1 μM IAA for 15 min. After staining,
850 hypocotyls were mounted in the same growth medium on microscopy slides and covered with
851 coverslips for imaging.

852 Hypocotyl imaging was performed using an Ultra High-Resolution Leica STELLARIS 8
853 confocal microscope equipped with a 20× water-immersion objective. Fluorescence signals
854 corresponding to the protonated form of HPTS were detected using excitation at 405 nm with an
855 emission peak at 514 nm, while signals from the deprotonated form were detected using excitation
856 at 458 nm with an emission peak at 514 nm.

857 For extracellular pH quantification, the ratio of fluorescence intensity excited at 458 nm to that
858 excited at 405 nm (458/405 ratio) was calculated. Approximately 5–6 independent hypocotyls were
859 analyzed per treatment, with about 2–3 cells analyzed per hypocotyl, resulting in a total of at least
860 15 cells per condition. Full cell boundaries were used for all measurements, and identical image
861 processing parameters were applied across all samples.

862 For *in vivo* HPTS calibration, hypocotyls were equilibrated in a measuring buffer (5 mM MES,
863 5 mM citric acid, 5M KOH, pH 2.5–7.5) for 30 min. The hypocotyls were then incubated in the
864 same buffer supplemented with 5 mM HPTS for 20 min. The hypocotyls were subsequently
865 mounted on a microscopy slide with the same buffer, covered with a coverslip, and imaged using
866 the same confocal settings as described above. A calibration curve was generated and pH values
867 were determined by fitting experimental data with a polynomial function.

868 ***In vivo* phosphorylation assay**

869 For the *in vivo* phosphorylation assay, 4-day-old light-grown seedlings were first subjected to
870 darkness for 12 h, followed by 1 μM IAA treatment for 10 min and then harvested and flash frozen
871 in liquid nitrogen. Samples were ground into a fine powder in liquid nitrogen and suspended in
872 2×SDS loading buffer (8% SDS, 100 mM Tris-HCl (pH6.8), 20% Glycerol, 0.02% BPB)
873 supplemented with protease inhibitor cocktail (A32955, Thermo Fisher Scientific, China). The

homogenates were boiled at 99°C for 3 min and then centrifuged at 12,000 g for 10 min at room temperature. Equal amounts of supernatant were loaded onto 4%–12% (w/v) SDS–PAGE gels to assess the levels of AHA2 (anti-AHA2 1:1000 dilution, PY231, Beijing QiWei YiCheng Tech Co., Ltd) and phosphorylation at Thr947 (anti-pThr947, 1:1500 dilution, ZW075213, Abmart, China). Goat anti-rabbit IgG and goat anti-mouse IgG (1:5000 dilution) were used as secondary antibodies. The signals were detected using the Tanon-2500R imaging system (Tanon, China).

Protein structure prediction and small-molecule docking

Protein structure prediction and small-molecule docking were performed using AlphaFold3 (v.3) (Abramson et al., 2024) and Chai-1 (v0.6.1) (Boitreaud et al., 2024), respectively, both in multimeric mode with default parameters. Structural models were visualized using PyMOL (v.3.0.3) (Shelton, 2025), and contact plots were generated using custom scripts. For AlphaFold structural prediction, LLG1 (24–168 AA) and ABP1 (34–198 AA) (full length with the signal peptide removed) were used. For Chai-1 docking analysis, LLG1 (24–149 AA) and ABP1 (34–198 AA) were used.

QUANTIFICATION AND STATISTICAL ANALYSIS

All experiments were independently repeated at least three times. Data are presented as mean ± SD. Statistical analyses were performed using GraphPad Prism 8 software. In all graphs, asterisks indicate statistical significance (n.s., not significant, $*P < 0.05$; $**P < 0.01$; $***P < 0.001$; $****P < 0.0001$) tested by Student's *t*-test (two groups), and lowercase/uppercase letters indicate statistical significance tested between multiple groups by one/two-way ANOVA at $P < 0.05$ (lowercase) or $P < 0.01$ (uppercase). The intensity of protein bands in Western blotting was quantified using ImageJ software.

References

Abramson, J., Adler, J., Dunger, J., Evans, R., Green, T., Pritzel, A., Ronneberger, O., Willmore, L., Ballard, A.J., Bambrick, J., et al. (2024). Accurate structure prediction of biomolecular interactions with AlphaFold 3. Nature *630*, 493-500. https://doi.org/10.1038/s41586-024-07487-w.

Adler, J., and Parmryd, I. (2010). Quantifying colocalization by correlation: The Pearson correlation coefficient is superior to the Mander's overlap coefficient. Cytometry A *77A*, 733-742. https://doi.org/10.1002/cyto.a.20896.

Amali, A.J., Awwad, N.H., Rana, R.K., and Patra, D. (2011). Nanoparticle assembled microcapsules for application as pH and ammonia sensor. Anal. Chim. Acta *708*, 75-83. https://doi.org/10.1016/j.aca.2011.10.001.

Barkawi, L.S., Tam, Y.-Y., Tillman, J.A., Pederson, B., Calio, J., Al-Amier, H., Emerick, M., Normanly, J., and Cohen, J.D. (2008). A high-throughput method for the quantitative analysis of indole-3-acetic acid and other auxins from plant tissue. Anal Biochem. *372*, 177-188. https://doi.org/10.1016/j.ab.2007.08.009.

Bellstaedt, J., Trenner, J., Lippmann, R., Poeschl, Y., Zhang, X., Friml, J., Quint, M., and Delker, C. (2019). A Mobile Auxin Signal Connects Temperature Sensing in Cotyledons with Growth Responses in Hypocotyls. Plant Physiol. *180*, 757-766. https://doi.org/10.1104/pp.18.01377.

Boitreaud, J., Dent, J., McPartlon, M., Meier, J., Reis, V., Rogozhnikov, A., and Wu, K. (2024). Chai-1: Decoding the molecular interactions of life. bioRxiv 2024.10.10.615955. https://doi.org/10.1101/2024.10.10.615955.

Bücherl, C.A., Bader, A., Westphal, A.H., Laptenok, S.P., and Borst, J.W. (2014). FRET-FLIM applications in plant systems. Protoplasma *251*, 383-394. https://doi.org/10.1007/s00709-013-0595-7.

Chen, L., Tong, J., Xiao, L., Ruan, Y., Liu, J., Zeng, M., Huang, H., Wang, J.-W., and Xu, L. (2016). YUCCA-mediated auxin biogenesis is required for cell fate transition occurring duringde novoroot organogenesis in Arabidopsis. J. Exp. Bot. *67*, 4273-4284. https://doi.org/10.1093/jxb/erw213.

Clough, S.J., and Bent, A.F. (2008). Floral dip: a simplified method forAgrobacterium-mediated transformation ofArabidopsis thaliana. Plant J. *16*, 735-743. https://doi.org/10.1046/j.1365-313x.1998.00343.x.

Gao, Y., Zhang, Y., Zhang, D., Dai, X., Estelle, M., and Zhao, Y. (2015). Auxin binding protein 1 (ABP1) is not required for either auxin signaling or Arabidopsis development. Proc. Natl. Acad. Sci. USA *112*, 2275-2280. https://doi.org/10.1073/pnas.1500365112.

Gomord V, D.L., Fitchette-Lainé AC, Satiat-Jeunemaitre B, Hawes C, and Faye L. (1997). The C-terminal HDEL sequence is sufficient for retention of secretory proteins in the endoplasmic reticulum (ER) but promotes vacuolar targeting of proteins that escape the ER. Plant J. *11*, 313-325. https://doi.org/10.1046/j.1365-313x.1997.11020313.x.

Zuo, J., Niu, Q. and Chua, N. (2000). An estrogen receptor-based transactivator XVE mediates highly inducible gene expression in transgenic plants. Plant J. *24*, 265-273. https://doi.org/10.1046/j.1365-313x.2000.00868.x.

Kakei, Y., Yamazaki, C., Suzuki, M., Nakamura, A., Sato, A., Ishida, Y., Kikuchi, R., Higashi, S., Kokudo, Y., Ishii, T., et al. (2015). Small-molecule auxin inhibitors that target YUCCA are powerful tools for studying auxin function. Plant J. *84*, 827-837. https://doi.org/10.1111/tpj.13032.

Kriechbaumer, V., Breeze, E., Pain, C., Tolmie, F., Frigerio, L., and Hawes, C. (2018). Arabidopsis Lunapark proteins are involved in ER cisternae formation. New Phytol. *219*, 990-1004. https://doi.org/10.1111/nph.15228.

Li, C., Yeh, F.L., Cheung, A.Y., Duan, Q., Kita, D., Liu, M.C., Maman, J., Luu, E.J., Wu, B.W., Gates, L., et al. (2015). Glycosylphosphatidylinositol-anchored proteins as chaperones and co-receptors for FERONIA receptor kinase signaling in Arabidopsis. Elife *4,* e06587. https://doi.org/10.7554/eLife.06587.

Lin, W., Zhou, X., Tang, W., Takahashi, K., Pan, X., Dai, J., Ren, H., Zhu, X., Pan, S., Zheng, H., et al. (2021). TMK-based cell-surface auxin signalling activates cell-wall acidification. Nature *599*, 278-282. https://doi.org/10.1038/s41586-021-03976-4.

Liu, F., Qu, P.Y., Li, J.P., Yang, L.N., Geng, Y.J., Lu, J.Y., Zhang, Y., and Li, S. (2024). Arabidopsis protein S-acyl transferases positively mediate BR signaling through S-acylation of BSK1. Proc. Natl. Acad. Sci. USA *121*, e2322375121. https://doi.org/10.1073/pnas.2322375121.

Liu, Z., Chu, X., Ren, W., Cheng, L., Liu, C., Wang, C., Gao, S., Dai, S., and Li, C. (2025a). PCP-B peptides and CrRLK1L receptor kinases control pollination via pH gating of aquaporins in Arabidopsis. Dev. Cell *60*, 1336-1347. https://doi.org/10.1016/j.devcel.2024.12.026.

Shelton, V. (2025). Determining the Effectivity of PyMOL Approaches Through the Experimental Evaluation of Lactoferrin Binding.

Sun, N., Wang, J., Gao, Z., Dong, J., He, H., Terzaghi, W., Wei, N., Deng, X.W., and Chen, H. (2016). Arabidopsis SAURs are critical for differential light regulation of the development of various organs. Proc. Natl. Acad. Sci. USA *113*, 6071-6076. https://doi.org/10.1073/pnas.1604782113.

Sylvain Merlot, N.L., Francesca Fenzi, Christiane Valon, Miguel Costa, Laurie Piette, Alain Vavasseur,

Bernard Genty, Karine Boivin, Axel Mu¨ ller, Je´roˆme Giraudat and Jeffrey Leung (2007). Constitutive activation of a plasma membrane Hþ-ATPase prevents abscisic acid-mediated stomatal closure. EMBO J. *26*, 3216-3226. https://doi.org/10.1038/sj.emboj.7601750.

Yang, Z., Xia, J., Hong, J., Zhang, C., Wei, H., Ying, W., Sun, C., Sun, L., Mao, Y., Gao, Y., et al. (2022). Structural insights into auxin recognition and efflux by Arabidopsis PIN1. Nature *609*, 611-615. https://doi.org/10.1038/s41586-022-05143-9.